Spatial Localization in Dissipative Systems

E. Knobloch

Department of Physics, University of California, Berkeley, California 94720; email: knobloch@berkeley.edu

Keywords

pattern formation, spatial dynamics, homoclinic snaking, front motion, pinning, structure growth

Abstract

Spatial localization is a common feature of physical systems, occurring in both conservative and dissipative systems. This article reviews the theoretical foundations of our understanding of spatial localization in forced dissipative systems, from both a mathematical point of view and a physics perspective. It explains the origin of the large multiplicity of simultaneously stable spatially localized states present in a parameter region called the pinning region and its relation to the notion of homoclinic snaking. The localized states are described as bound states of fronts, and the notions of front pinning, self-pinning, and depinning are emphasized. Both one-dimensional and two-dimensional systems are discussed, and the reasons behind the differences in behavior between dissipative systems with conserved and nonconserved dynamics are explained. The insights gained are specific to forced dissipative systems and are illustrated here using examples drawn from fluid mechanics (convection and shear flows) and a simple model of crystallization.

1. INTRODUCTION

Spatially localized structures are frequently observed in physical systems. Interest in such structures dates back to the discovery of solitary waves by John Scott Russell, who followed such a wave for one or two miles along the Union Canal near Edinburgh, Scotland, in 1834. Korteweg & de Vries (1) developed an explanation of such waves using long wave theory, but only in 1965 when Zabusky & Kruskal (2) discovered that these waves retain their particle-like identity despite collision—except for a phase shift arising from their interaction—were solitons born. Solitons are structures associated with completely integrable partial differential equations and are therefore a property of (some) conservative or dissipationless systems. In this review, we focus instead on solitary structures arising in forced dissipative systems owing to spontaneous localization. Such systems are not integrable, and the mathematics behind the presence of dissipative solitons, as they are sometimes called, is quite different. As a result their properties are quite distinct from those associated with true solitons.

This article is devoted to explicating the basic properties of localized structures in dissipative systems from the point of view of both basic physics and basic mathematics, and to illustrating their properties using a variety of different systems. In particular, we emphasize the important role played by the Swift-Hohenberg equation in developing useful intuition that can be transferred to more complex systems. In selecting this focus, the article seeks to remain simultaneously orthogonal to two other applications-oriented reviews (3, 4) as well as to Reference 5. A number of open issues concerning spontaneous localization in dissipative systems is listed in Reference 6; many of these remain open. We do not consider spatial localization such as Anderson localization that arises in linear inhomogeneous systems. We begin with two examples.

1.1. Solitons on the Surface of a Ferrofluid

A ferrofluid is a suspension of small magnetic dipoles held apart by a surfactant. The free surface of this fluid undergoes a buckling instability, called the Rosensweig instability, when a uniform DC magnetic field of sufficiently large strength is applied in a direction normal to the surface (7). This instability results in a hexagonal array of stationary peaks. This instability is strongly subcritical, leading to a broad region of magnetic field strengths for which a hexagonal pattern coexists stably with the flat surface. Experiments reveal that within this region there is a subregion where multiple localized states can be created (8). This can be done by bringing a bar magnet toward the surface, pulling out a peak, and removing the bar magnet. Remarkably, in this subregion the peak remains, and the process can therefore be repeated, pulling out more and more peaks. **Figure 1***a* shows an example of a structure created in this way. Note that these structures are created by suitably tailored finite amplitude perturbations: When the perturbation is removed the system relaxes, but an imprint of the perturbation remains. This relaxation process dissipates energy, although no dissipation takes place within the localized state that remains. Thus, at every point in this subregion a number of different states, consisting of one, two, three, or more peaks, coexists with the flat and hexagonal states, and all are simultaneously stable, as summarized in a bifurcation diagram in **Figure 1***b* showing the surface energy E_s as a function of the applied vertical magnetic field B. Thus, multiple localized states are associated with the presence of a classic hysteresis loop between a pair of states, one of which is homogeneous and the other structured.

1.2. Cellular Buckling in Long Structures

Hunt et al. (9) showed that when a tall structure, in their case a cylindrical shell, is loaded axially, the buckling of the structure may be confined to the midsection. The instability sets in at a critical
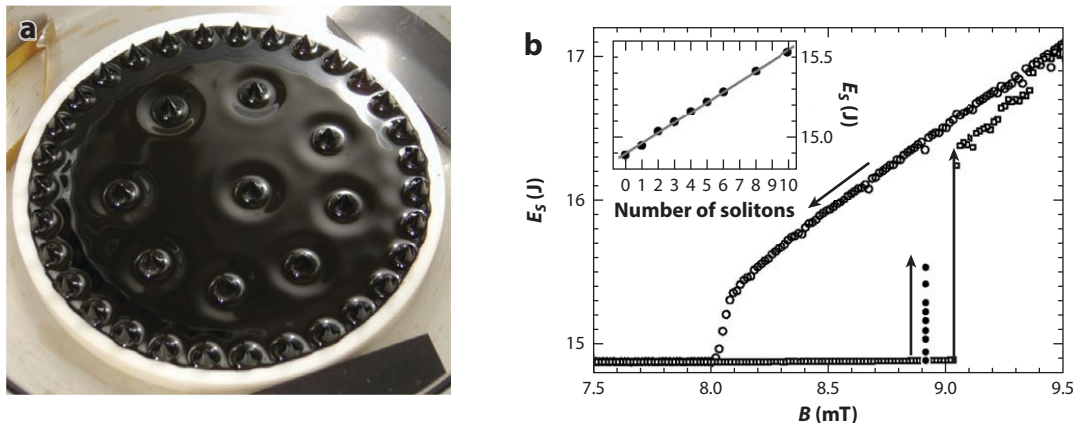
Figure 1

(*a*) Two-dimensional localized structures on the surface of a ferrofluid. (*b*) The corresponding bifurcation diagram showing the surface energy E_s as a function of the applied magnetic field B. Stable steady states with $n = 1, 2, \ldots$ peaks are present at $B = 8.9$ mT. Adapted with permission from Reference 8.

load Λ_c, where the unbuckled state loses stability in a strongly subcritical bifurcation, meaning that loads $\Lambda > \Lambda_c$ lead to catastrophic collapse. However, for $\Lambda < \Lambda_c$ the instability generates a sequence of steady buckled states, shown in **Figure 2a** in terms of a bifurcation diagram specifying the response of the system (**Figure 2a**, *horizontal axis*) as a function of the load Λ (**Figure 2a**, *vertical axis*). The internal stress and displacement patterns that result are both cellular (**Figure 2b**), but the structures that form are weaker than the unbuckled state in the sense that they can support only smaller loads. In fact, most of these states are unstable: An infinitesimal increase in the load brings about the collapse of the structure. However, some of these buckled states, lying on the portions of the curve with positive slope, are stable and can again support an increasing load. If this load becomes too large, however, no stable state is present and the structure collapses further, leading to a sequence of stable buckled states, as indicated by the arrows in **Figure 2a**. These differ in the number of rows of cells or dimples that form: Each stable section adds a pair of rows of cells, one on either side of the preexisting cells. These solutions are organized around a special value of the load parameter Λ, called the Maxwell load. The significance of this parameter value will become apparent as we proceed.

The key issues to understand are the origin of the large multiplicity of simultaneously stable states and their persistence over a range of parameter values within the hysteresis loop. In mathematics, this persistence is called structural stability.

1.3. Other Examples

In the above examples, dissipation allows us to reach a stable localized structure (the structures are attractors), but dissipation ceases when the steady state is reached. Other localized structures are characterized by a balance between energy input and energy dissipation within the structure. Examples include cavity solitons (3, 10), DC gas discharges (4, 11), an optical light valve with feedback (12), a number of convection systems (13, 14), shear flows (15–17), neural systems (18), and reaction-diffusion systems (19, 20), as well as models of the processes leading to desertification (21, 22) and the formation of crime hot spots (23). Time-dependent localized states called oscillons present in chemical systems (24) and in vibrated granular media (25) or liquids (26) are a closely related phenomenon. Systems with a conserved quantity exhibit distinct behavior, as discussed
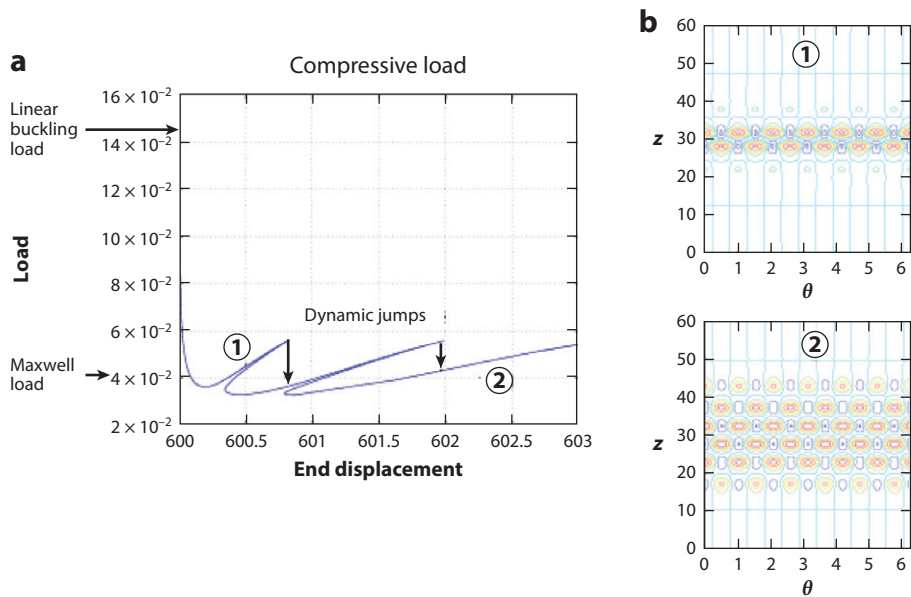
a Compressive load

b

Figure 2

(*a*) Bifurcation diagram for the buckling of an axially loaded cylinder. (*b*) Sample buckled states at locations indicated in panel *a*. Adapted with permission from G. Lord.

further below. A variety of fronts and defects in spatially periodic structures also falls into this category: If the background pattern is removed by demodulation, the structure that is left is localized, with its own dynamics.

Given this vast area, this review is necessarily selective. Consequently, after explaining the basic ideas behind the ubiquitous presence of localized structures, we describe just three applications: to different types of convection, to shear flow instability, and to a simple model of crystallization from a supercooled liquid.

2. THEORY

In this section, we assume the system is described by a local partial differential equation in one spatial dimension (1D) for a real variable $u(x, t)$, $u_t = g(u, u_x, u_{xx}, \ldots)$, and suppose that this equation is reversible in space, i.e., that it is equivariant with respect to $R_1 : x \to -x, u \to u$. Thus, $R_1 g R_1 = g$ and $g(u, u_x, u_{xx}, \ldots) = 0$ is a reversible dynamical system in space, with phase space $(u, u_x, u_{xx}, \ldots) \in \mathbb{R}^n$, whose solutions represent steady states. Owing to reversibility, n is even. Of particular interest is the fixed point O, with coordinates $u = u_x = \ldots = 0$. This point represents a spatially homogeneous state, and this state must have at least one unstable and one stable direction in space in order that a solitary wave be present with the property $u \to 0$ as $|x| \to \pm\infty$. Thus, a necessary condition for the existence of solitary waves biasymptotic to the homogeneous state O is that O is a hyperbolic fixed point in phase space. To determine the conditions for this to be so, we must examine the spatial eigenvalues of O. For this purpose, we linearize $g = 0$ around O,

$$g_u(0)u + g_{u_x}(0)u_x + g_{u_{xx}}(0)u_{xx} + \ldots = 0, \qquad\qquad 1.$$

and look for solutions of the form $u \propto \exp \lambda x$. The spatial eigenvalues λ are thus given by

$$P(\lambda) = 0,$$

2.

where P is real-valued so that $P(\lambda) = 0 \Rightarrow P(\bar{\lambda}) = 0$. In addition, reversibility implies that $P(-\lambda) = 0$. Thus, if $u = 0$ has two negative real eigenvalues it also has two positive real eigenvalues. Likewise, if λ is a complex root of $P(\lambda) = 0$, then so are $-\lambda$ and $\pm\bar{\lambda}$, and the eigenvalues form a quartet in the complex plane. It follows that in spatially reversible systems, P is in fact a function of λ^2, and the simplest nontrivial case yields $P(\lambda) \equiv \lambda^4 - b\lambda^2 + a = 0$. **Figure 3** depicts the location of the four eigenvalues of the spatial problem in the complex plane as a function of the coefficients a and b. Below the curve $C_2 \cup C_3$, the eigenvalues lie on the axes, implying that either their real part or their imaginary part is zero. Above this curve the eigenvalues form a complex quartet. We focus on the transition occurring at C_2. In the region labeled 4 in **Figure 3**, all the eigenvalues lie on the imaginary axis, implying that the eigenmodes are purely oscillatory in space. As a or b increases, the eigenvalues collide on the curve C_2 and move into the complex plane forming a quartet. This transition provides the key to the appearance of spatially localized states.

When nonlinear terms are retained, the invariant subspace spanned by the unstable eigenvectors turns into an invariant manifold called the unstable manifold $W^u(O)$, and the stable eigenspace turns into the stable manifold $W^s(O)$. These manifolds are tangent to the corresponding eigenspaces at O, and their dimensions correspond to the numbers n_u and n_s of unstable and stable eigenvalues of O, respectively. If these manifolds intersect, it is possible to find a trajectory that leaves $u = 0$ as x increases from $-\infty$ and returns to $u = 0$ as $x \to \infty$, i.e., a spatially localized solution. This is more likely if the dimensions of these manifolds are high.
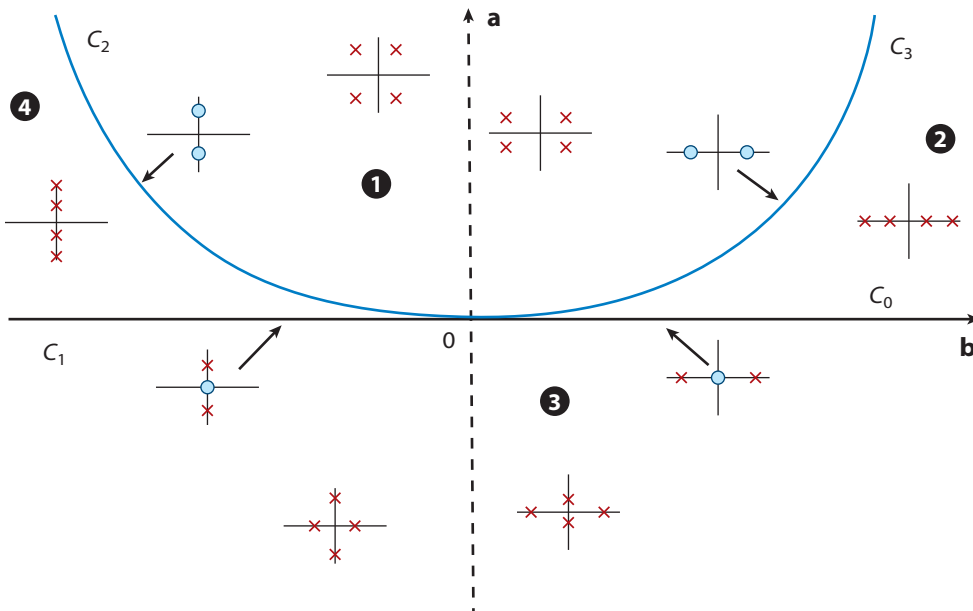

Figure 3

Roots of the equation $\lambda^4 - b\lambda^2 + a = 0$ in the a,b plane, showing four distinct types of behavior labeled 1–4. Adapted from Reference 27.

The following examples for $n = 4$ are helpful.

- Suppose $g = 0$ has a hyperbolic fixed point O with $n_{u,s}(O) = 2$. If $n = 4$ the intersection of $W^u(O)$ and $W^s(O)$ is generically of codimension one, i.e., we expect homoclinics $O \to O$ at isolated parameter values only. But in a reversible system the codimension is zero and localized states are structurally stable.
- Suppose $g = 0$ has a pair of hyperbolic fixed points O and O' fixed by R_1 with $n_u(O) = 2$ and $n_s(O') = 2$. If $n = 4$, the intersection of $W^u(O)$ and $W^s(O')$ is generically of codimension one, i.e., we expect (stationary) fronts $O \to O'$ at isolated parameter values only. If g is reversible we have a codimension one heteroclinic cycle $O \to O' \to O$.
- Suppose $g = 0$ is reversible with a hyperbolic fixed point O with $n_{u,s} = 2$ and a hyperbolic periodic orbit γ, both fixed by R_1. Owing to the symmetry R_1, the orbit γ has one stable and one unstable Floquet multiplier plus two $+1$ multipliers. Its center-stable eigenspace is therefore three dimensional, and $W^s(\gamma)$ is therefore also three dimensional. Thus, the intersection between $W^u(O)$ and $W^s(\gamma)$ is of codimension zero and therefore structurally stable, i.e., fronts $O \to \gamma$ are robust. Moreover, if this is the case, $g = 0$ will have a robust heteroclinic cycle $O \to \gamma \to O$. Such cycles persist under parameter changes and play an important role in what follows because homoclinic orbits $O \to O$ that pass m times around γ accumulate on them as $m \to \infty$.

Note that robust cycles of this type are not possible in second-order systems ($n = 2$).

2.1. The Paradigm: Swift-Hohenberg Equation

The expectations derived from these geometrical ideas are helpful in interpreting numerical results obtained on specific systems. The most studied, and in many ways prototypical, system is the Swift-Hohenberg equation, originally suggested as a description of pattern formation in Rayleigh-Bénard convection (28, 29), written here in d dimensions:

$$u_t = r u - \left(q_c^2 + \nabla^2\right)^2 u + f(u).$$ 3.

Here, $f(u)$ represents a bistable nonlinearity of the form $f(u) = b_2 u^2 - u^3$; we refer to the resulting equation as SH23. The parameters r and q_c represent the bifurcation parameter and a characteristic wavenumber (inverse length scale). In unbounded domains, the wavenumber q_c can be set equal to $q_c = 1$, but this is not the case on finite domains. In addition, Equation 3 has the minimum number of spatial derivatives identified above for the presence of robust heteroclinic cycles. As a result, we use it as a "normal form" for understanding systems exhibiting spatially localized structures.

Equation 3 has a variational structure, i.e., it possesses a Lyapunov functional $F[u(x, t)]$, such that

$$u_t = -\frac{\delta F[u]}{\delta u(x, t)},$$ 4.

where F is given by

$$F = \int_{-\infty}^{\infty} \mathrm{d}^d x \left[-\frac{1}{2} r u^2 + \frac{1}{2}\left[\left(q_c^2 + \nabla^2\right)u\right]^2 - \int_0^u f(v)\mathrm{d}v \right].$$ 5.

It follows that

$$\frac{dF}{dt} = -\left(\frac{\partial u}{\partial t}\right)^2 \leq 0 \qquad\qquad 6.$$

and hence that $dF/dt < 0$ provided $\partial u/\partial t \neq 0$ somewhere in the domain. Thus, on a finite domain with null boundary conditions, all solutions evolve toward stationary states; on an unbounded domain solutions in the form of steadily moving fronts are possible. In the following, we think of the functional $F[u]$ as the (free) energy of the system. Stable/unstable solutions correspond to local minima/maxima of this energy. We shall see that in appropriate parameter regimes the energy landscape described by the free energy (5) can be exceedingly complex.

2.1.1. The temporal view. The usual way to examine the stability of the state $u = 0$ is to linearize Equation 3 about this state and look for solutions of the form $u \propto \exp(\sigma t + iqx)$, where σ is the growth rate of a perturbation with wavenumber q. The growth rate σ is given by the dispersion relation

$$\sigma = r - \left(q_c^2 - q^2\right)^2. \qquad\qquad 7.$$

The marginal stability curve is determined by setting $\sigma = 0$ and then minimizing the marginal value $r = r(q)$ with respect to the wavenumber q. This calculation leads to the prediction $r_c = 0$ for the onset of instability and of the associated wavenumber $q = q_c$ (**Figure 4**).

Observe that for $r < 0$ the condition for marginal stability, $r = \left(q_c^2 - q^2\right)^2$, has no solution for real q, but it does have a solution with q complex. In contrast, if $r > 0$, there is a pair of real solutions, $q = q_\pm$, with $q_- < q_c < q_+$. As r decreases to zero from above, the wavenumbers $q_\pm$ approach $q = q_c$ from opposite directions, and at $r = 0$ they collide at $q = q_c$. Thus, the minimum of the marginal stability curve is in fact associated with the collision of two roots of the marginal dispersion relation, i.e., a 1:1 spatial resonance (**Figure 4**).
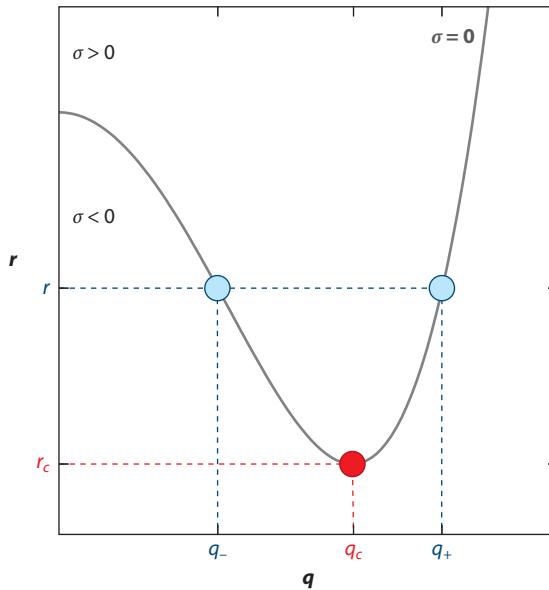

Figure 4

The neutral stability curve and the 1:1 spatial resonance. Adapted with permission from C. Beaume.

2.1.2. The spatial view. We can appreciate what is happening if we focus on steady states from the outset. Steady solutions of the linear problem lie on the neutral stability curve $r = \left(q_c^2 + \lambda^2\right)^2$, where λ is the spatial eigenvalue of the homogeneous state O: $u = u_x = u_{xx} = u_{xxx} = 0$. For $r < 0$, the spatial eigenvalues of O form a complex quartet (**Figure 5a**). At $r = 0$ these eigenvalues collide pairwise on the imaginary axis (**Figure 5b**), and for $r > 0$ they split but remain on the imaginary axis (**Figure 5c**). Thus, the temporal and spatial points of view are closely related: The onset of instability in the temporal point of view is equivalent to the presence of a pair of purely imaginary spatial eigenvalues $\lambda = \pm i q_c$ of double multiplicity.

It is useful to look at the transition at $r = 0$ in a little more detail. We write $r = \epsilon^2 \mu$, where $\mu = \mathcal{O}(1)$ and $\epsilon \ll 1$. We then find that for $\mu < 0$, the spatial eigenvalues are $\lambda = \pm \epsilon(2q_c)^{-1}\sqrt{-\mu} \pm i\left[q_c + \mathcal{O}\left(\epsilon^2\right)\right]$, whereas for $\mu > 0$ the eigenvalues are $\lambda = \pm i\epsilon(2q_c)^{-1}\sqrt{\mu} \pm i\left[q_c + \mathcal{O}\left(\epsilon^2\right)\right]$. These considerations suggest that when $r < 0$ the solutions near $u = 0$ will be growing or decaying as $u \sim \exp(\pm\epsilon\sqrt{-\mu}\,x/2q_c)$, i.e., that the amplitude of such solutions will vary on a long scale $X \equiv \epsilon x$ while their wavenumber remains close to q_c. This analysis suggests that near $r = 0$ solutions take the form

$$u(x) = \epsilon u_1(x, X) + \epsilon^2 u_2(x, X) + \ldots, \qquad 8.$$

where

$$u_1(x, X) = Z(X; \epsilon)e^{iq_c x} + c.c. \qquad 9.$$

Normal form description of the reversible 1:1 spatial resonance (30) shows that the resulting calculation must be taken to fifth order in ϵ. However, the third-order truncation is already informative (31, 32):

$$4\,q_c^2\,Z'' = -\mu\,Z + 4\,q_c^2\,a|Z|^2 Z + \mathcal{O}(\epsilon). \qquad 10.$$

In order that the primary instability be subcritical, the coefficient $a \equiv \left(3/4q_c^2\right)\left(1 - 38b_2^2/27q_c^4\right) < 0$. In the subcritical region $\mu < 0$, there are therefore two types of solutions: a constant solution,

$$Z(X) = \left(\frac{\mu}{4\,q_c^2\,a}\right)^{1/2} e^{i\phi} + \mathcal{O}(\epsilon), \qquad 11.$$

corresponding to a periodic state,

$$u_\gamma(x) = \left(\frac{r}{4\,q_c^2\,a}\right)^{1/2} \cos(q_c x + \phi) + \mathcal{O}(r), \qquad 12.$$

Figure 5
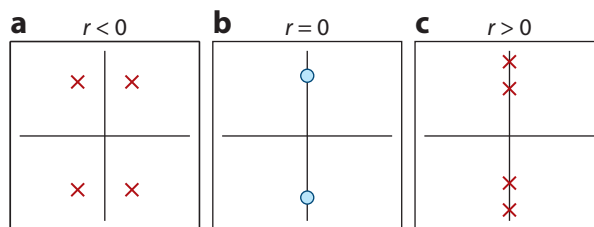
The behavior of the spatial eigenvalues λ of $u = u_x = u_{xx} = u_{xxx} = 0$. (a) $r < 0$. (b) $r = 0$. (c) $r > 0$.

and a spatially localized solution,

$$Z(X) = \left(\frac{\mu}{2 q_c^2 a}\right)^{1/2} \text{sech}\left(\frac{X \sqrt{-\mu}}{2 q_c}\right) e^{i\phi} + \mathcal{O}(\epsilon), \qquad 13.$$

corresponding to

$$u_L(x) = 2\left(\frac{r}{2 q_c^2 a}\right)^{1/2} \text{sech}\left(\frac{x \sqrt{-r}}{2 q_c}\right) \cos(q_c x + \phi) + \mathcal{O}(r). \qquad 14.$$

For the periodic states, the spatial phase ϕ is arbitrary; this is not so for the localized states for which the spatial phase ϕ is locked to $\phi = 0, \pi$ when terms beyond all orders are retained (33, 34). Thus, in SH23 there are two branches of localized states that bifurcate from $u = 0$ at $r = 0$ (hereafter, $L_{0,\pi}$), each of which is symmetric with respect to the spatial reflection R_1. Both bifurcate subcritically. There are no localized states when $a > 0$.

If the above calculation is taken to fifth order in ϵ (31, 32), one learns one additional important fact: the existence [under appropriate conditions (30)] of a Maxwell point at which the periodic state γ with wavenumber q_c and the homogeneous state $u = 0$ have equal energy. This point corresponds to the presence of a heteroclinic cycle between the states represented by $Z = 0$ and $Z = $ const., i.e., a pair of back-to-back fronts between the homogeneous state $u = 0$ and the periodic state of infinite length. The calculation also shows that homoclinic orbits to O consisting of finite lengths of the periodic state between pairs of fronts accumulate on this heteroclinic cycle. This fact reveals a problem: The asymptotic expansion indicates that the heteroclinic cycle is present at a single parameter value, the Maxwell point, whereas the geometric considerations described earlier lead to the expectation that this cycle should persist over an interval of parameter values. The resolution is subtle and demands computations beyond all orders, i.e., the retention of exponentially small terms in the expansion parameter ϵ (35, 36), sometimes referred to as non-adiabatic terms (37). As noted by Pomeau (38), the phase ϕ in Equation 14 cannot be arbitrary since one should not be able to move the envelope arbitrarily relative to the periodic oscillation: The envelope itself depends on position. The resulting pinning of the front to the periodic state behind it leads to a pinning potential that prevents the motion of fronts between the $u = 0$ state and the periodic state with wavenumber q_c unless the parameter r is changed sufficiently that the energy difference between the two states exceeds the pinning potential. Detailed analysis of the exponentially small terms in the parameter regime $r = \mathcal{O}(\epsilon^4)$, $|a| = \mathcal{O}(\epsilon^2)$ reveals the presence of multiple localized states within an exponentially thin region near the Maxwell point. These states exhibit behavior that has been termed homoclinic snaking (39): The two branches of $\phi = 0$, and $\phi = \pi$ states (i.e., of symmetric homoclinic states $L_{0,\pi}$) are intertwined (35, 36).

To appreciate the significance of these results, we need to examine what happens when $|a| = \mathcal{O}(1)$ and r decreases deeper into the subcritical region.

2.2. Snakes-and-Ladders Structure of the Pinning Region: SH23

Figure 6 shows the L^2 norm $\|u\|_2^2 \equiv \int_{-\infty}^{\infty} u^2(x)dx$ of the localized states $L_{0,\pi}$ in SH23 as a function of the bifurcation parameter r. The L^2 norm (per unit length) of the periodic state, labeled γ, is shown for comparison. The figure shows that the two branches of even-parity localized states that bifurcate subcritically from $u = 0$ at $r = 0$ enter a shaded region—hereafter, the snaking or pinning region—in which they undergo repeated saddle-node bifurcations as they snake across the region. These saddle-nodes converge exponentially rapidly to a pair of r values—hereafter, $r(E_-)$ and
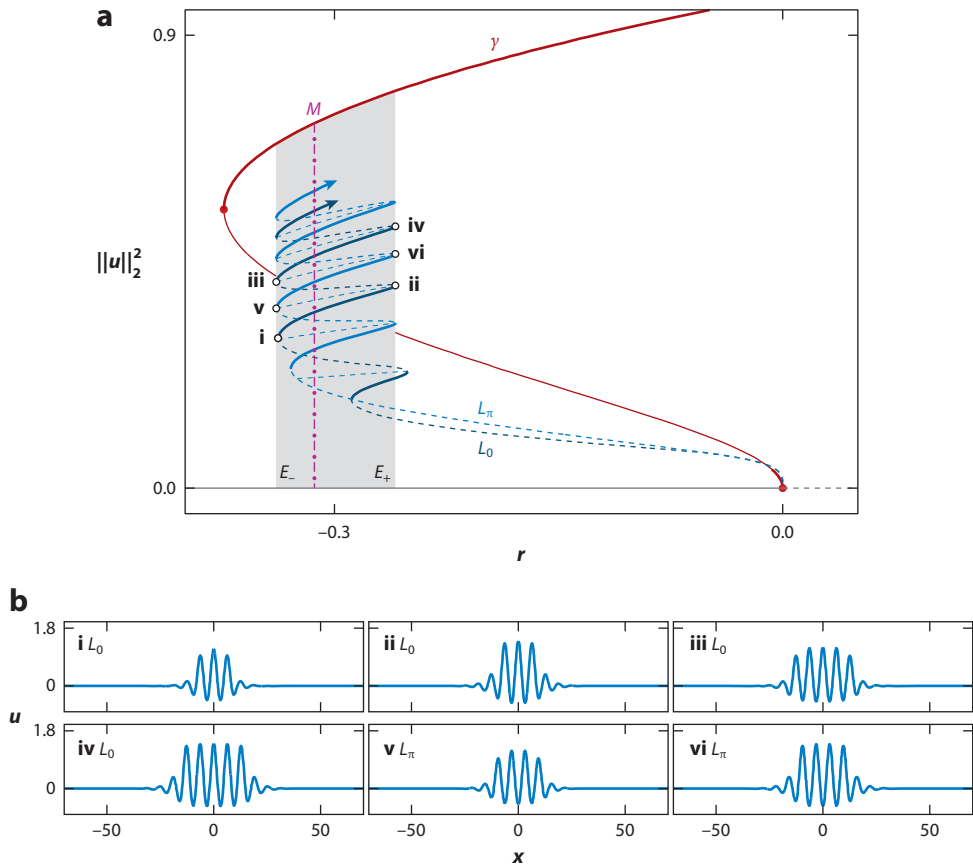
Figure 6

(*a*) Bifurcation diagram showing the snakes-and-ladders structure of localized states in SH23. Away from
the origin the snaking branches L_0 and L_π are contained within a snaking region (*shaded*) between
E_- and E_+, where $r(E_-) \approx -0.3390$ and $r(E_+) \approx -0.2593$. Solid lines indicate stable states. Dotted lines
indicate unstable states. (*b*) Sample localized profiles $u_L(x)$: Panels *i–iv* lie on L_0 at the 3rd–6th
saddle-nodes from the bottom; Panels *v–vi* lie on L_π. Parameters: $b_2 = 1.8$, $q_c = 1$. Adapted
from References 31 and 40.

$r(E_+)$—representing the boundaries of the shaded region. The convergence is monotonic and from
the right in both cases. The lower panels show a series of profiles of $u_L(x)$ along $L_{0,\pi}$. These reveal
that states L_0 are characterized by a peak in the center, whereas states L_π have a dip in the center. As
one proceeds up either branch, each localized state nucleates a pair of peaks, one on either side, in
the vicinity of $r = r(E_-)$. These grow to the amplitude of the coexisting periodic state γ by the time
one reaches the next fold on the right, at $r = r(E_+)$, and the branch turns around to repeat the
process. Thus, as one proceeds up the intertwined $L_{0,\pi}$ branches the localized states repeatedly add
peaks on either side while preserving their parity, each back-and-forth oscillation increasing the
width of the state by two wavelengths $2\pi/q_c$. On the real line, this process continues indefinitely as
both branches approach the periodic state γ.

Figure 7*a* is a close-up view of **Figure 6**, focusing on the rung states that connect the $L_{0,\pi}$ snak-
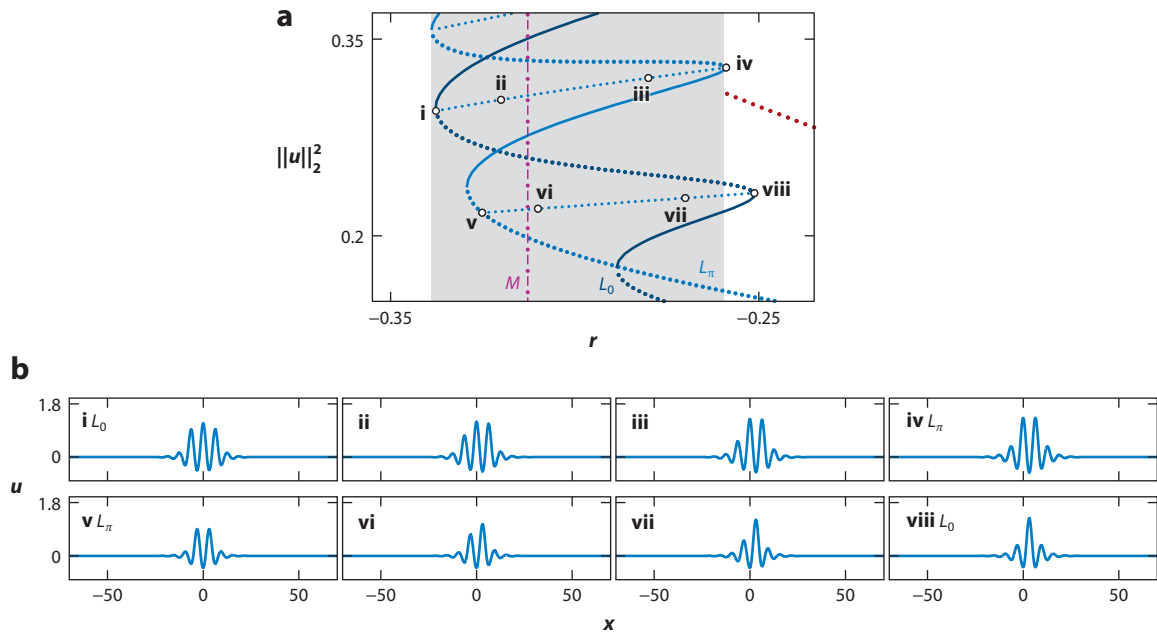ing branches. These states are asymmetric with respect to the reflection $x \to -x$ (**Figure 7*b***)

Figure 7

(*a*) Close-up view of **Figure 6a** showing two rungs connecting the snaking branches L_0 and L_π. Solid lines indicate stable states. Dotted lines indicate unstable states. (*b*) The profiles *i* and *viii* lie on L_0, whereas *iv* and *v* lie on L_π. The remaining profiles are asymmetric and lie on the rungs. Adapted from References 31 and 40.

but stationary. The rungs are created in pitchfork bifurcations that break the R_1 symmetry of the $L_{0,\pi}$ states. Consequently, each rung in the figure corresponds to two states related by R_1 and hence of identical L^2 norm.

The stability of these states may be found by linearizing about the different states and solving the resulting eigenvalue problem for the temporal growth rate σ. It turns out that only two modes are of interest: the reflection-symmetric amplitude mode whose growth rate passes through zero at every fold and the antisymmetric phase mode that triggers the bifurcation to asymmetric states. As one follows either branch to the large L^2 norm, the zeros of the amplitude and phase modes approach each other exponentially rapidly (with the latter always on the unstable side of the fold) implying that asymptotically the rung states bifurcate from the folds (31). In this limit, the odd and even modes may be written in the form $v(L) \mp v(-L)$ to within terms of order $e^{-\alpha L}$, $\alpha = \mathcal{O}(1)$, where $v(L)$ is the marginal eigenfunction localized at the front at $x = L$ and $2L$ is the (large) length of the localized state (41, 42). In this regime, the localized structure $u_L(x)$ can thus be considered to be a bound state of a pair of fronts. The rung states are always unstable. The resulting stability assignments are indicated in **Figures 6** and **7**. A neutral translation mode is present in addition.

2.2.1. Multipulse states. In fact, the situation is much more complicated. This is because the snaking region also contains a variety of multipulse states (40). The term multipulse refers to the fact that the phase space trajectory comes close to O after the first localized state (pulse) but only

forms a homoclinic orbit to O after two (two-pulse) or more (multipulse) excursions. Multipulse states should be thought of as (weakly) bound states of two or more localized structures of the type we have been discussing.

Multipulse states can be equispaced, forming a periodic array of identical localized structures. Such states are not very different from single-pulse states if the pulses are sufficiently separated, and it comes as no surprise that they also snake (**Figure 8**). But one can also find two-pulse states consisting of identical pulses that are separated by a distance that is less than the average interpulse spacing. The locations of such pulses are "quantized" in terms of half wavelengths, π/q_c. Specifically, two identical L_0 pulses can have a local maximum or a local minimum at the halfway location between them (40, 43). On a periodic domain of a large but finite period, there is thus a finite number of such states. These do not snake but instead lie on nested isolas. The nested isolas are in turn organized into a vertical stack, each level consisting of nested isolas of bound states of localized states of ever-increasing length (**Figure 9**). The breakup of the two-pulse states into isolas as soon as they are not evenly spaced is a consequence of the resulting asymmetry in the interaction between adjacent pulses.

In addition, one can also find two-pulse states consisting of different localized states (40) and an ever greater variety of multipulse states. Thus, the snaking region consists of an immense variety of different localized structures, a significant fraction of which can be stable. All correspond to critical points of the energy F, stable ones to local minima, and unstable ones to local maxima. Thus, the energy landscape in the pinning region has a remarkably complex structure.

2.2.2. Mathematical explanation of the pinning region.
For applications it is important to understand what determines the width of the pinning or snaking region. For this purpose, it is helpful
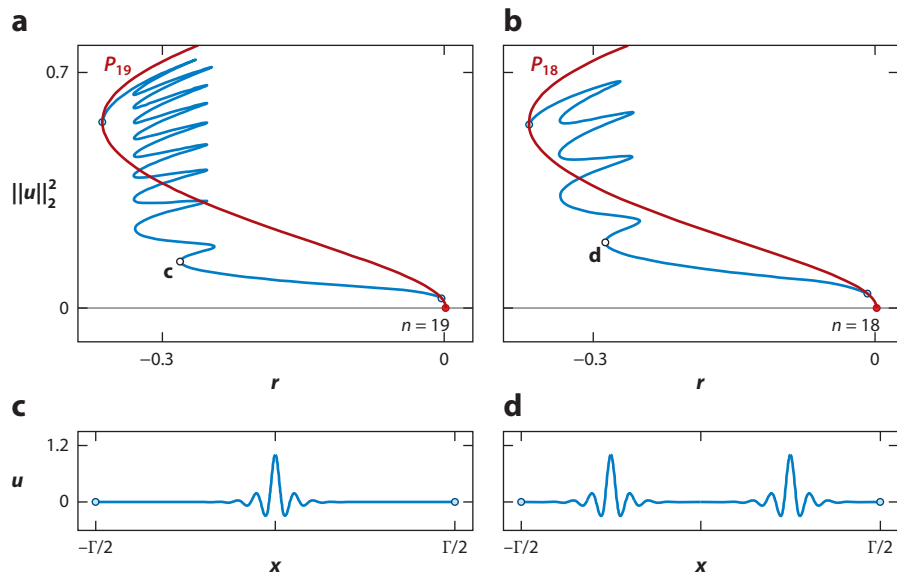

Figure 8

Bifurcation diagrams for SH23 showing (*a*) a L_0 single-pulse snaking branch and (*b*) a two-pulse snaking branch consisting of two evenly spaced copies of L_0, both on the same periodic domain of period Γ. (*c*,*d*) Sample profiles at the points indicated in the bifurcation diagrams; the states in panel *d* are separated by $\Gamma/2$. Similar branches consisting of L_π pulses are omitted. Parameters: $b_2 = 1.8$, $q_c = 1$, $\Gamma = 118$. Adapted from Reference 40.
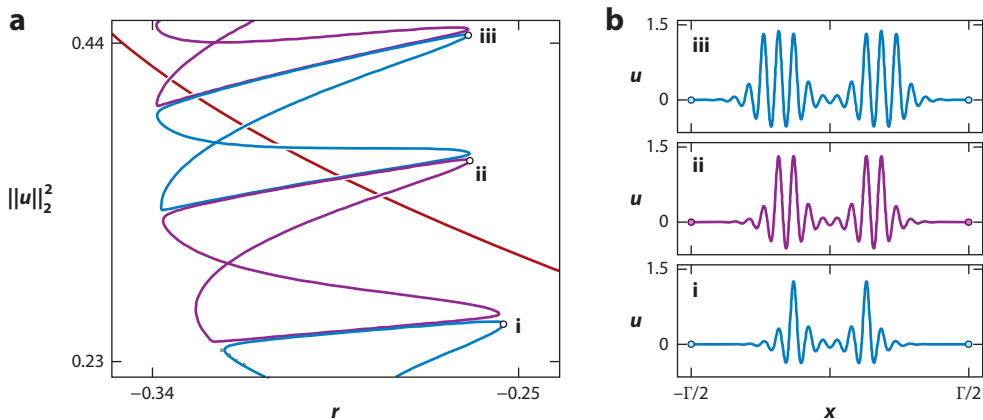
Figure 9

(*a*) Bifurcation diagram showing isolas of symmetric but unevenly spaced two-pulse states in SH23. In the main diagram, only one isola at each level of the isola stack is plotted to avoid clutter. (*b*) Profiles at the points labeled in the bifurcation diagram; the states are separated by distances less than $\Gamma/2$. Parameters: $b_2 = 1.8$, $q_c = 1$, $\Gamma = 118$. Adapted from Reference 40.

to observe that equilibria of Equation 3 satisfy a fourth-order ordinary differential equation in space that defines a (nonintegrable) autonomous Hamiltonian system with Hamiltonian

$$H = -\frac{1}{2}\left(r - q_c^4\right)u^2 + q_c^2 u_x^2 - \frac{1}{2}u_{xx}^2 + u_x u_{xxx} - \int_0^u f(v)dv. \qquad 15.$$

Thus, $dH/dx = 0$, and any homoclinic orbit $O \to O$ must lie in the level set $H = 0$, i.e., in a three-dimensional surface in four dimensions. This is so for the heteroclinic cycle $O \to \gamma \to O$ as well.

Because of translation invariance, periodic orbits of Equation 3 are not isolated—for each H there is a continuous family of such orbits. In the following, we pick $H = 0$ and select one representative from this family, for example, by assigning the origin $x = 0$ to the maximum value of u along the orbit. We call the resulting orbit γ. A point on this orbit with phase ϕ relative to $x = 0$, $\gamma(\phi)$ is a fixed point of a "time-T" map, where T is the (spatial) period of the orbit, and we may pick ϕ to correspond to a point of symmetry on γ, for example, $\phi = 0$ (39). Note that T depends in general on H. By construction, the "time-T" map is two dimensional and has two fixed points, O and $\gamma(\phi)$. The result of repeated application of the "time-T" map can therefore be represented in a plane, as shown in **Figure 10**. The figure shows the two fixed points as solid black points; these lie on a purple line labeled $Fix(R_1)$, representing solutions with the symmetry R_1. The figure shows the intersections of the stable and unstable manifolds of O, labeled $W^{s,u}(O)$, with the surface $H = 0$. In **Figure 10**, these are one dimensional (*blue curves*) and consist of points that approach O after an infinite number of forward and backward applications of the map. The intersection of the corresponding (three-dimensional) center-stable and center-unstable manifolds of γ with $H = 0$ at phase $\phi = 0$ is shown in brown and is also one dimensional. Since we are dealing with a discrete map, these manifolds consist of discrete sequences of points obtained by applying the map to different points in the stable and unstable manifolds of these fixed points. Because of the discrete nature of the resulting two-dimensional dynamics, we expect the unstable manifold $W^u(O)$ to intersect transversally with the center-stable manifold $W^s(\gamma)$ (**Figure 10**, *top right panel*). The point of intersection is simultaneously on both manifolds, implying that forward iterations take it to
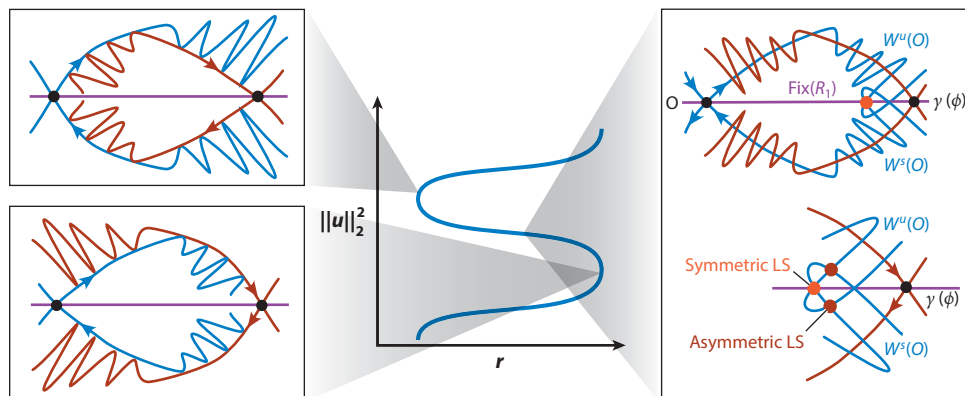
Figure 10

A graphic of the stable and unstable manifolds of the fixed points O and $\gamma(\phi)$ in the planar representation, at different values of r in the pinning region. Intersections of $W^u(O)$ and $W^s(O)$ correspond to localized states (LS) homoclinic to O. Adapted from Reference 41. ©2009 Society for Industrial and Applied Mathematics. Adapted with permission. All rights reserved.

$\gamma(\phi)$, whereas backward iterations take it to O, i.e., such a point is a heteroclinic point. Each image of this point, forward or backward, is also a heteroclinic point since it must again lie on an intersection of these manifolds. Since the forward iterates accumulate on γ, the unstable manifold $W^u(O)$ must execute increasingly wild gyrations near $\gamma(\phi)$, as indicated in **Figure 10**. This is a consequence of the Hamiltonian nature of the steady states of Equation 3, which implies that the "time-T" map is area-preserving. Thus, the areas of the (primary) lobes are all the same, and since the foot of the lobes shrinks toward $\gamma(\phi)$, their length must grow in proportion. Spatial reversibility implies that $W^s(O)$ undergoes identical behavior and hence that $W^u(O)$ and $W^s(O)$ must intersect. The primary intersections must lie on the purple curve and hence correspond to solutions with $u(-x) = u(x)$ that lie simultaneously in $W^u(O)$ and $W^s(O)$ (**Figure 10**, *large red dot*). Such solutions represent symmetric homoclinic solutions of Equation 3. Observe that because the primary intersections accumulate on $\gamma(\phi)$, there is in fact an infinite number of such homoclinic solutions corresponding to symmetric localized structures of ever greater length. **Figure 10** also indicates that associated with each primary intersection there is a pair of secondary intersections (**Figure 10**; *bottom right panel*, *small red dots*). These do not lie in the purple line and hence correspond to asymmetric homoclinic points, i.e., the rung states.

Figure 10 shows that the heteroclinic tangle described above is created, as the bifurcation parameter r increases, at the point of first tangency between $W^u(O)$ and $W^s(\gamma)$ (**Figure 10**, *top left panel*), and destroyed at the point of last tangency (**Figure 10**, *bottom left panel*). Thus, the snaking region is bounded on either side by the location of tangencies between these manifolds, and no (long) localized states are present outside of the parameter interval between these two tangencies (19, 39, 41).

An essentially identical picture applies to reversible but non-Hamiltonian systems since the fundamental properties of the heteroclinic tangle depend only on the presence of a transversal intersection between $W^u(O)$ and $W^s(\gamma)$ together with spatial reversibility. For this reason, the geometrical picture sketched here has a far greater applicability than one may imagine at first sight. This is a consequence of the fact that a transversal intersection between manifolds cannot be destroyed by small perturbations in the parameter r, or, indeed, of the equation, i.e., it is a consequence of structural stability.

2.2.3. Physical explanation of the pinning region. Consider now the energetics of the system. The free energy F allows us to compare the energy of the homogeneous state O with that of the periodic state γ. The point where these are equal is called the Maxwell point by analogy with a phase transition between two homogeneous phases such as a liquid and a gas. At the Maxwell point the two phases coexist; away from it one or the other is energetically favored, and a front separating the two will move so as to lower the energy of the system. In the present case, $F(O) < F(\gamma)$ when $r < r_M$, implying that O is energetically preferred and vice versa when $r > r_M$. However, the phase γ is structured and small changes in r do not result in front motion, as the front is held back by a pinning potential due to the structured state behind it (38). This self-pinning allows stationary fronts over a range of r straddling r_M, and r must be changed by a finite amount to overcome the pinning potential and allow the fronts to move. Within this interval many steady states coexist since it costs little to insert fronts between the two competing phases. The pinning region can thus be thought of as an "unfolding" of the Maxwell point due to the heterogeneity of one of the states.

The wavelength $\ell(r)$ of the pattern within the localized structure depends on the value of r in the pinning region. This wavelength is not given by minimizing the free energy F because of the $H = 0$ constraint required of all homoclinic orbits. One finds that for $r < r_M$, the wavelength is compressed relative to that at r_M, but that it is stretched for $r > r_M$. This behavior is expected on energy grounds (to reduce energy the fronts are displaced inward for $r < r_M$ and outward for $r > r_M$) and is in agreement with predictions based on the imposition of the $H = 0$ constraint (31, 44).

We remark that the presence of the fronts at either end of the structure leads to a unique wavenumber between them, however far apart the fronts are. This is in contrast to spatially periodic states for which there is an interval of stable wavenumbers within the so-called Eckhaus stability limits (45, 46). Thus, the fronts collapse the Busse balloon (45, 46).

2.3. Depinning

If r is moved sufficiently far from r_M, the energy difference between O and γ exceeds the pinning potential and the fronts depin (19). The resulting motion can be predicted by projecting SH23 onto the near-marginal eigenfunctions present at either edge of the pinning region. As already mentioned, the marginally stable amplitude eigenfunctions are localized near either front of the structure. Near E_+, where the state of the system evolves toward the lower energy periodic state, this fact indicates incipient nucleation of new cells just outside the localized state. Direct integration of Equation 3 reveals time-dependent growth of the structure via sequential nucleation of new cells (**Figure 11a**). The nucleation time depends on the distance from the edge of the pinning region, as indicated in **Figure 11b**. The time diverges at the edge of the pinning region (where it takes an infinite amount of time to nucleate a new cell) and decreases as the distance from the pinning region increases. The speed of the front, which is a pushed front because it propagates into a stable state (47), can be calculated from the time it takes to nucleate cells at the front (31, 48). To the left of the pinning region (where the solution evolves toward the lower energy zero state), the fronts move inward via sequential annihilation of cells with the same dependence on the distance from E_- as in the E_+ case (31).

2.4. Broken Symmetries

The scenario described above is substantially affected by forced symmetry-breaking, as we now describe.
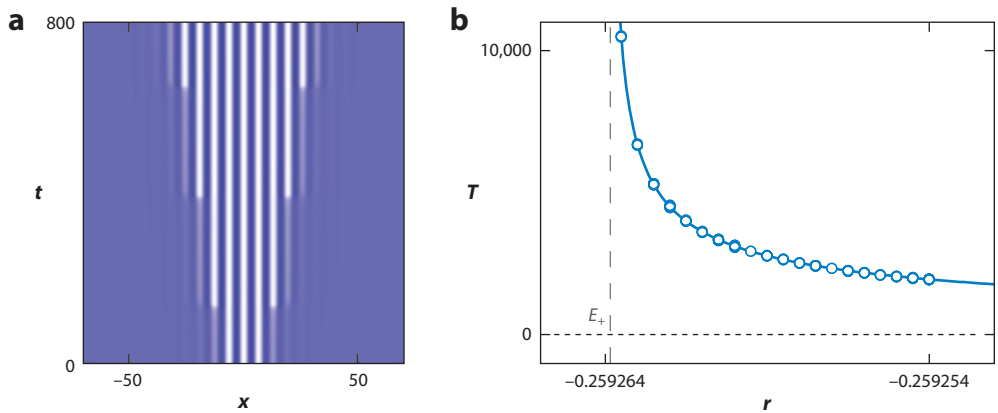
Figure 11

Space-time plot of (*a*) the evolution of a localized structure in SH23 and (*b*) the nucleation time T as a function of r. Parameters: $b_2 = 1.8$, $q_c = 1$. Adapted from Reference 44.

2.4.1. Finite size effects. **Figure 8a** is computed on a periodic domain of length Γ with periodic boundary conditions. We see that for $\Gamma < \infty$, the multiple bifurcation at $r = 0$ breaks up into a primary bifurcation to a periodic wavetrain and a secondary bifurcation from this state to the (two) branches of localized states that takes place at small but nonzero amplitude. This is almost certainly the reason why spatially localized states have been discovered only recently: Almost all textbooks on hydrodynamic instability immediately impose periodic boundary conditions when studying the instability of a homogeneous base state. This innocuous assumption pushes the bifurcation to localized states to finite amplitude, where its discovery requires not only knowledge of the finite amplitude periodic state but also a linear stability analysis of a nontrivial periodic state requiring Floquet theory. As we have seen, the problem becomes so much easier if posed on the real line.

Figure 8a also reveals that on a finite periodic domain snaking does not continue forever. Once the localized structure has grown to fill the domain no additional growth is possible, and the branch of localized states exits the snaking region and terminates near the fold on a branch of periodic states. The details of this transition are, in general, complex since they depend on exactly how much space is left, i.e., on Γ mod $\ell(r)$, where $\ell(r)$ is the wavelength within the pinning region (49). Moreover, as Γ increases the termination points must "jump" between different periodic states, a process studied in References 49 and 50. Near the fold the localized states resemble holes in an otherwise periodic wavetrain. This bifurcation is present even on the real line and gives rise to two branches of holes that snake once the hole approaches $u = 0$ and starts to broaden. On the real line, the branches of localized states bifurcating from $u = 0$ at $r = 0$ and the branches of holes remain distinct, but on a periodic domain with $\Gamma < \infty$ they connect up pairwise: A broad localized state can, after all, be viewed as a hole in a periodic state. Moreover, on smaller domains (**Figure 8b**), a single-pulse state bifurcates from the periodic states at a larger amplitude than on larger domains, and the resulting branch also terminates farther from the fold.

If the boundary conditions are changed from periodic to Robin (or mixed) boundary conditions, the effect is dramatic. Since periodic states are now absent, the localized states bifurcate directly from $u = 0$ in a primary bifurcation. Thereafter, they snake normally since the localized states are insensitive to the details of the boundary conditions, but when the domain is almost full the snaking branch evolves continuously into an extended large amplitude (almost) periodic state with defects at the boundaries (51, 52).

2.4.2. Broken reversibility.

Spatial reversibility can be broken, for example, by adding dispersion to SH23. In this case, one expects that generically all states drift. This expectation is confirmed by numerical calculations (53); these show in addition that dispersion destroys the snakes-and-ladders structure of the snaking region and that the drifting localized states now fall on a stack of figure-eight isolas. As the dispersion increases the isolas shrink and eventually disappear. Thus, drifting localized structures are absent for large dispersion.

2.4.3. Broken translation invariance.

Broken translation invariance, either through the imposition of Robin boundary conditions at the boundaries of a finite domain (51) or through space-dependent forcing (54, 55), have also been studied. The details are complex and not well understood. Either type of forcing selects preferred locations for the localized structures (56) and may result in incomplete snaking, depending on whether local maxima are in phase with the maxima in the localized state or out of phase. Large-scale heterogeneity may cause an overall slant to the snaking structure, as discussed in a different context below. We also mention that spatially periodic forcing can generate stable localized states even in systems in which snaking would not otherwise be present (57). In fact, this is always the case in the vicinity of a Maxwell point between two homogeneous states (58) and is a consequence of the pinning introduced into the system by the forcing. The related problem of localization on an imposed periodic lattice is of interest in optics (59).

Discrete problems in which the spatial Laplacian is replaced, for example, by nearest neighbor coupling, also lack translation invariance and constitute an important class of systems with multiple coexisting localized structures that snake (60).

2.5. Additional Symmetry

The Swift-Hohenberg equation with $f(u) = b_3 u^3 - u^5$ (hereafter, SH35) possesses an extra symmetry $R_2 : x \to x, u \to -u$ that is analogous to the so-called Boussinesq symmetry of Rayleigh-Bénard convection with identical boundary conditions at the top and bottom (61). For this reason, predictions based on SH35 find a number of applications, particularly in fluid mechanics. The most important properties of SH35 include the following: (*a*) The periodic states with $q = q_c$ bifurcate subcritically if $b_3 > 0$. (*b*) Exponentially small terms select four phases $\phi : 0, \pi/2, \pi, 3\pi/2$ (62, 63). The $\phi = 0, \pi$ states are related by R_2 and likewise for the $\phi = \pi/2, 3\pi/2$ states. A bifurcation diagram showing the L^2 norm of u_L thus shows two branches, a branch of even parity states $\phi = 0, \pi$, and a branch of odd parity states $\phi = \pi/2, 3\pi/2$. The former are invariant under R_1 as in SH23; the latter are invariant under $R_2 \circ R_1$. Both bifurcate subcritically from $u = 0$ at $r = 0$, as described by Equation 14 with $a = -3b_3/4q_c^2$. (*c*) The odd and even parity branches are organized within the same type of snakes-and-ladders structure as SH23, with identical stability properties (62). (*d*) Each back-and-forth oscillation of a branch indicates the nucleation of half a wavelength on either side of the localized structure.

2.6. Other Effects

A number of other effects has also been studied.

2.6.1. Nonvariational effects.

Gradient systems such as Equation 3 are nongeneric. Generic systems no longer possess an energy functional, but the snakes-and-ladders structure of the snaking or pinning region persists when a gradient system is perturbed by nongradient terms. However, whereas solutions with the symmetry R_1 remain stationary, the asymmetric rung states now drift; the drift direction is determined by the asymmetry. In addition, secondary bifurcations

may appear on the stable segments of the primary snaking branches leading to localized oscillations (64). As examples, we mention the generic pattern-forming model for biological, chemical, and optical systems derived in Reference 65 and a variety of two-species reaction-diffusion systems that are formally of fourth order in space. In particular, if these systems exhibit a primary instability to periodic states (e.g., a Turing instability) that is subcritical, the same basic ideas apply. Thus, snaking localized structures are found, for example, in the Gierer-Meinhardt model (20).

2.6.2. Collisions of localized structures. In nonvariational systems with the symmetry $R_2 \times R_1$, the odd parity states are fixed by $R_2 \circ R_1$. Such states are necessarily stationary. To see this, suppose that their speed $c \neq 0$. Application of R_1 yields a state with speed $-c$, but by R_2 this state is the same as the state with speed c. Thus, $c = 0$. However, secondary bifurcations that break either symmetry generate asymmetric drifting states. However, when R_2 is externally broken, odd parity states deform into asymmetric states that drift with a speed that depends on the solution length (42, 66). At the same time, even parity states persist and remain stationary. Since a large number of stable, coexisting, traveling states is created in this way, it is possible to study head-on collisions between identical states, head-on and follow-on collisions between distinct states, and collisions between traveling and stationary states (66). These collisions are attractive/repulsive if the approaching fronts are unlike/like, but all collisions are inelastic: The two states stick together, forming a final state that is either moving or stationary. The length of this state exceeds that of the incoming states because additional structure is nucleated between them during the collision (at least when $r > r_M$). **Figure 12** shows a typical space-time diagram for Equation 3 with $f(u) = b_3 u^3 - u^5 + \epsilon u_x^2$ and compares it with an analogous collision of binary fluid convectons (67). The behavior could not differ more from the dynamics of integrable systems exhibiting solitons.

2.6.3. Other growth mechanisms. In the preceding discussion, we have seen that the steady structures grow as one follows a solution branch by nucleating new cells along the periphery of the structure. Although this appears to be the most common process in the Swift-Hohenberg type of models and in many systems arising in fluid dynamics (see below), other mechanisms are also possible. In the forced complex Ginzburg-Landau equation (FCGLE) describing the 1:1 and 2:1 temporal resonance (68, 69), one finds a different mechanism, called defect-mediated snaking (70), whereby the central cell of the structure repeatedly splits, injecting spatial phase and pushing the preexisting cells to either side. The boundaries of the snaking region are determined by the Eckhaus instability (45, 46) of the periodic wavetrain, which changes the corresponding periodic orbit in phase space from a hyperbolic periodic orbit to an elliptical periodic orbit, thereby breaking the connection to this orbit. Details of this mechanism are described in Reference 71. Outside the pinning region, the structure grows in time, initially by repeated splitting of the central cell, but once it becomes broad enough, phase is injected at a pair of locations on either side of the center, which gradually migrate outward but never reach the location of the moving fronts (72).

We mention that the Lugiato-Lefever equation (LLE), which describes pattern formation in an optical cavity in a plane transverse to an incident coherent light beam (73), is a special case of the FCGLE with 1:1 resonance. A driven optical cavity is described by similar equations that reduce to SH23 in the limit of nascent bistability and weak dispersion (74).

2.6.4. Localized temporal dynamics. As mentioned above, the FCGLE provides a convenient reduction, under appropriate and well-understood conditions, of a temporally vibrated system to an autonomous partial differential equation (PDE). In this equation, uniform steady states correspond to spatially homogeneous oscillations, and localized steady states correspond to localized oscillations. Recent work (75) compares oscillons in a nonautonomous PDE with the corresponding

solutions of the FCGLE (69) and demonstrates just how robust the FCGLE approximation is. Localized solutions need not be periodic, however. Different examples of localized states with chaotic dynamics are known (68, 76). The much-studied chimera states in systems of identical globally coupled phase oscillators (77–79) provide an example in which a set of adjacent oscillators oscillates in phase while the phases of the remaining oscillators remain random. The turbulent stripes interspersed with laminar flow observed in experiments on plane Couette flow (PCF) provide another intriguing example (80), as do turbulent puffs in pipe flow (81) and turbulent boundary layer flow (82) (see below).

2.6.5. Noise. It is natural to consider the effect of small amplitude additive noise on the localized states in the pinning region. Each local minimum has a lowest barrier in the energy landscape across which escape is most probable. The type of evolution that results is expected to depend on
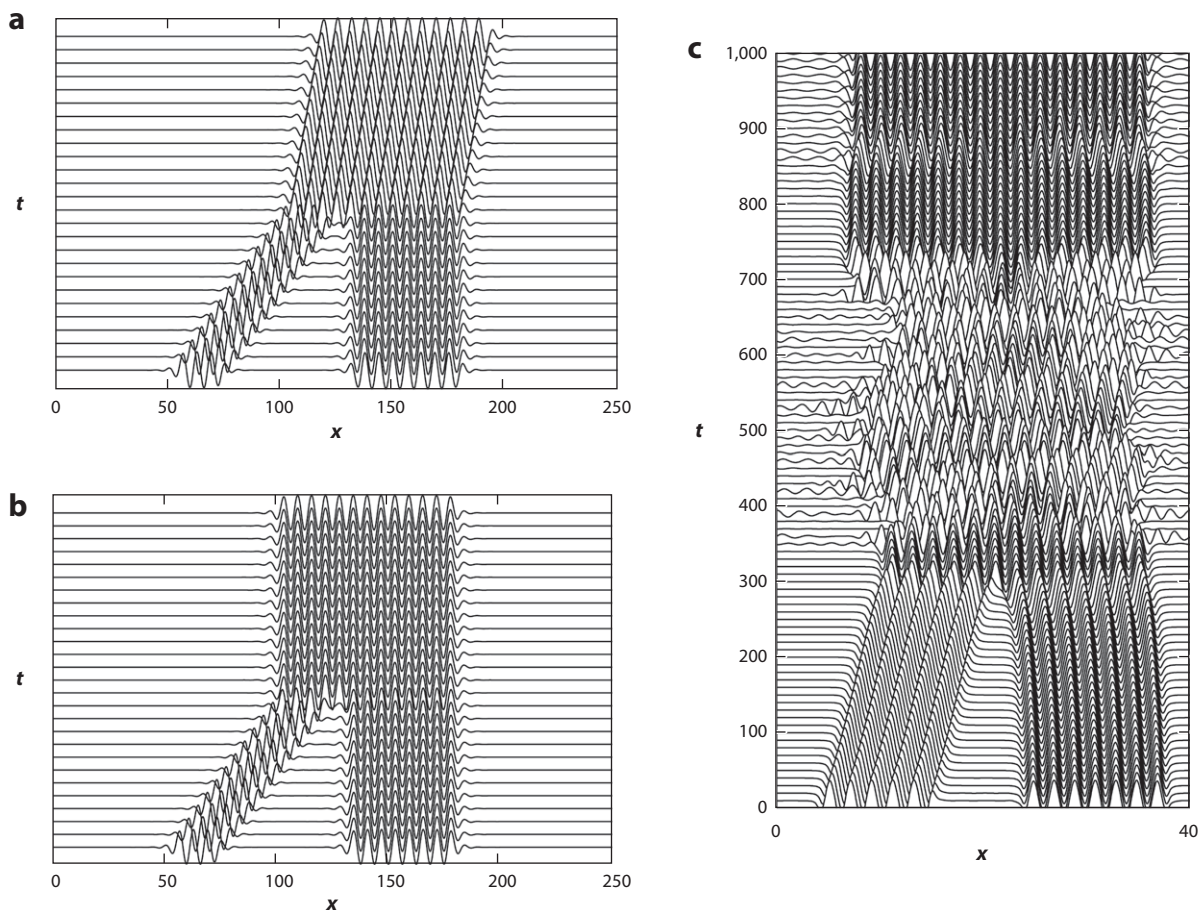
Figure 12

Space-time plot of (*a*) a repulsive collision and (*b*) an attractive collision between a traveling and a stationary localized state in the Swift-Hohenberg equation with $f(u) = b_3 u^3 - u^5 + \epsilon u_x^2$ and $r = -0.65$, $b_3 = 2$, $\epsilon = 0.1$. Adapted from Reference 66. (*c*) An attractive collision between traveling and stationary convectons in binary fluid convection, shown in terms of the midplane temperature fluctuation, is accompanied by wave radiation but is broadly similar. Adapted from Reference 67.

whether $r < r_M$ or $r > r_M$. In the former case, the localized structure should gradually shrink; in the latter case, it should gradually grow. Despite some numerical studies of this process (83, 84), the details of the resulting evolution are by no means clear. The effects of multiplicative noise have not been studied.

3. TWO-DIMENSIONAL LOCALIZED STRUCTURES

We now consider the Swift-Hohenberg equation 3 in two dimensions (2D). In 2D, there is a larger range of different types of localized structures that arise, including stripes, spots, targets, squares, and hexagons. Quadratic terms in $f(u)$ favor, as usual, patterns with hexagonal structure (45, 46).

3.1. Stripe-Like Patterns

Stripe patterns, produced by extending 1D localized states in the y direction, are the simplest 2D states to consider. In addition to the 1D instability modes already mentioned, the stripes are now susceptible to transverse (y-dependent) instabilities. There are two types, wall modes that represent instabilities confined to the fronts and body modes that represent bulk instability. Together these modes reduce substantially the region in parameter space where stable localized states are found (**Figure 13**). The 1D pinning region originates in the codimension-two points $(r, b_2) = \left(0, \sqrt{27/38}q_c^2\right)$ (SH23) and $(r, b_3) = (0, 0)$ (SH35). However, because of transverse instabilities, the region of stable stripes does not reach all the way to these codimension-two points (32).

Outside the 2D stability region, the transverse instabilities may remain confined to the fronts; may propagate throughout the interior of the stripe, leaving behind a stripe with a 2D internal structure; or may depin the fronts, resulting in a dynamic invasion of the stable homogeneous state (32). The time-independent SH35 stripes with 2D fronts (**Figure 14a**) have been followed using numerical continuation (85). One finds two types of growth: The structure grows in a 1D manner by adding rolls parallel to the existing rolls, or it may grow by sending out rolls that are orthogonal to the existing rolls. In the former process, the fronts connecting the state to the background are pinned to the structured state behind them, and this
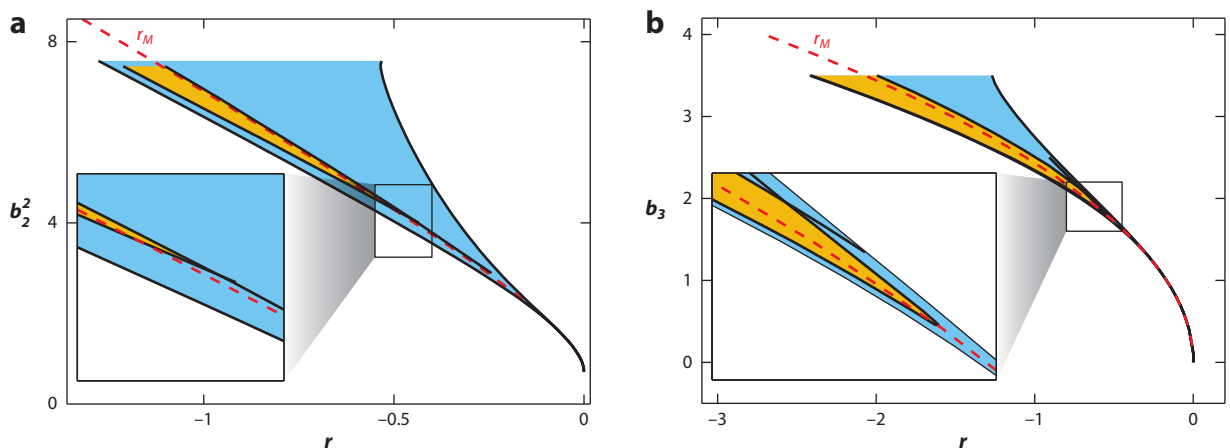
Figure 13

Stability regions for localized stripes with respect to one- (*blue*) and two-dimensional (*gold*) perturbations in (*a*) SH23 and (*b*) SH35, both for $q_c = 1$. Adapted from Reference 32.
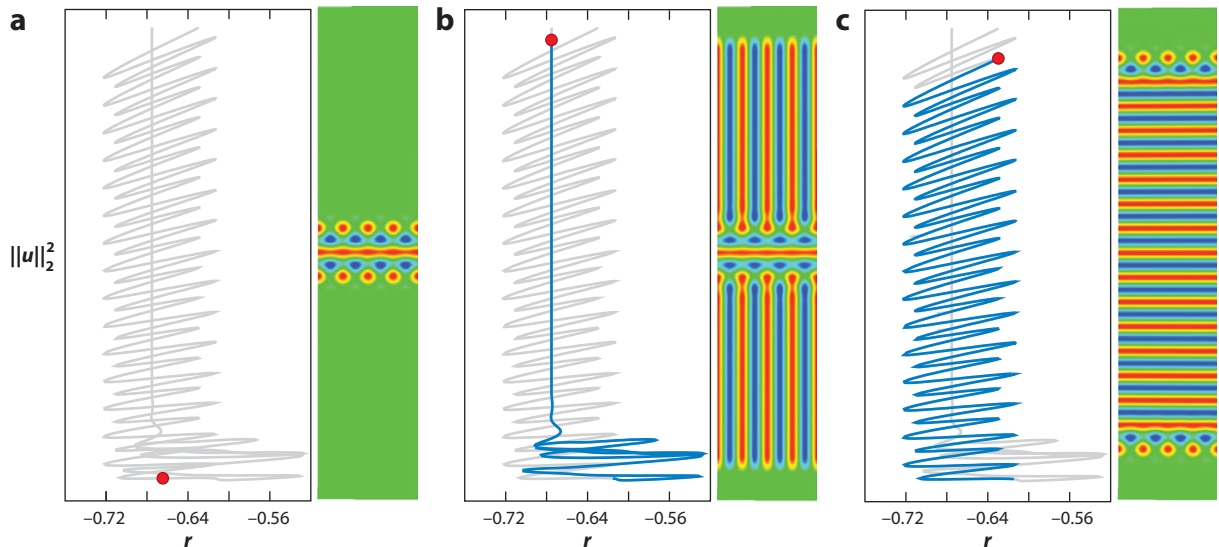
Figure 14

Bifurcation diagram of an even parity localized stripe pattern in SH35. (*a*) A localized state identified through time integration. (*b*,*c*) Different types of snaking obtained by following the solution in panel *a* in opposite directions. Each figure shows the appropriate portion of the bifurcation diagram (*left panel*) and the solution profile $u(x, y)$ (*right panel*) corresponding to the location indicated by the red dot. Parameters: $b_3 = 2$, $q_c = 1$. Adapted from Reference 85. ©2010 Society for Industrial and Applied Mathematics. Reprinted with permission. All rights reserved.

type of growth process is therefore accompanied by snaking (**Figure 14*c***). In the latter process, the fronts see behind them a translation invariant state, and hence no pinning takes place and the L^2 norm of the state therefore grows monotonically (**Figure 14*b***). This type of collapsed snaking is typical of the approach to the Maxwell point between two homogeneous phases. However, the pinning process continues to generate intertwined branches of states with odd and even parity, with asymmetric rung states connecting even states to odd, even states to even, and odd states to odd, the latter two of which may be stable. Additional states with checkerboard internal structure are located on stacks of isolas.

3.2. Structures Localized in Two Dimensions

To identify structures fully localized in 2D, we may perform analogs of the experiment in Reference 8. We introduce distinct localized perturbations in different parts of the domain and allow them to relax. In the right parameter regime, these may relax to a localized spot or target pattern, or to a localized patch of hexagons (SH23; **Figure 15**); in SH35, we may instead get a stripe-like pattern localized in both directions. We show examples of the former in **Figure 16** and of the latter in **Figures 17** and **18**. For other examples, see Reference 19.

The growth process whereby the hexagonal patch grows as the solution branch is followed has been studied in detail in Reference 86: The structure first adds a cell (or two cells) in the center of each face and then fills in the row by adding cells symmetrically on either side of the new cell. The last locations to be filled are the six corners of the structures. These nucleation events are all reflected in the associated snaking diagram. Why the structure grows in this manner is not understood, although the misalignment of the folds provides an indication of the energy associated
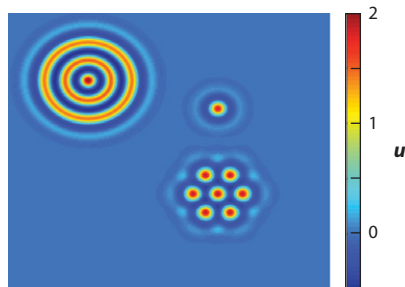
Coexisting localized structures generated by different finite amplitude perturbations of the $u = 0$ state in SH23. Parameters: $r = -0.5$, $b_2 = 2.2$, $q_c = 1$. Adapted from Reference 86. ©2008 Society for Industrial and Applied Mathematics. Reprinted with permission. All rights reserved.

with the nucleation of cells in different locations along the edges. There are two different types of hexagonal structures confined to a stripe, with wavenumbers $(k_0, k_1, k_2) = (1, 0, 0)$ and $(0, 1, 1)$ relative to the front, and these also grow in specific ways (86) and in particular exhibit secondary snaking (see below).

The 2D localized stripes shown in **Figures 17** and **18** are also poorly understood. One presumes that it is the curvature of the states in **Figure 17** that pins the curved fronts and prevents them from expanding outward. The structures shown in **Figure 18** are locally concave and hence cannot be explained in terms of the usual notions of surface energy. In fact, stable localized structures with no symmetry can be created by cutting out pieces of symmetric states—in appropriate parameter regimes, the resulting structure is stable and does not heal over time.

Figure 19 summarizes the location of some of the states mentioned above in the parameter plane for SH23. As in 1D, the pinning regions are exponentially narrow near $r = 0$ and so have not been extended all the way to the vertical axis.
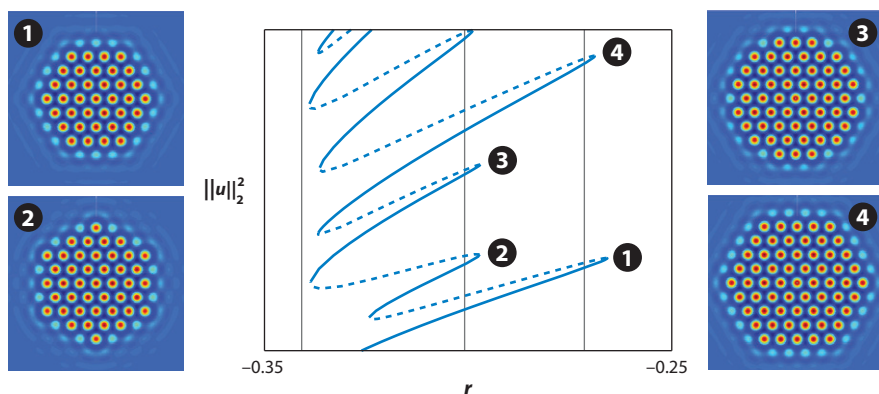

Figure 16

Bifurcation diagram for localized hexagons in SH23 showing the L^2 norm as a function of the bifurcation parameter r. The side panels illustrate the solution profiles at the points labeled in the middle panel. Solid lines indicate stable solutions. Dashed lines indicate unstable solutions. Parameters: $b_3 = 1.6$, $q_c = 1$. Adapted from Reference 86. ©2008 Society for Industrial and Applied Mathematics. Reprinted with permission. All rights reserved.
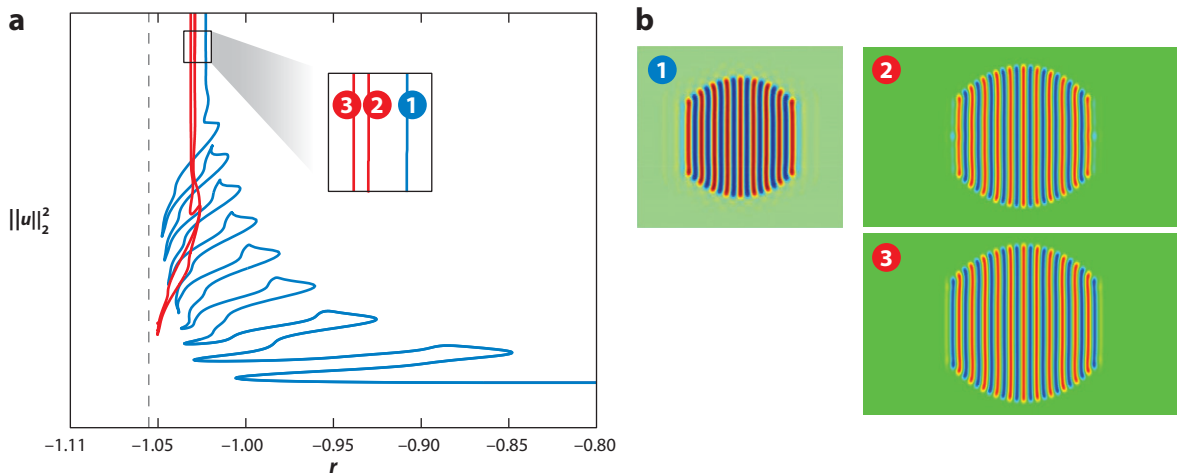
Figure 17

(*a*) Barrel-shaped localized structures of SH35 initially snake, but large structures of this type lead to collapsed snaking. (*b*) Subsidiary barrel-shaped structures differing by one stripe at the points labeled in panel *a*. Parameters: $b_3 = 2.50081$, $q_c = 1$. Adapted from Reference 85. ©2010 Society for Industrial and Applied Mathematics. Reprinted with permission. All rights reserved.

3.3. Spots and Targets

Figure 15 reveals the presence of two distinct types of steady axisymmetric structures: spots and targets. The spatial dynamics formulation of the axisymmetric problem leads to a nonautonomous problem in the radial coordinate R. Despite this (nontrivial) complication, it is possible to obtain the following results for SH23 (87, 88): (*a*) For each $b_2 > 0$, there is a family of spots (called spot A) with a positive $\mathcal{O}(|r|^{1/2})$ amplitude in the center for small $|r|$, resembling Bessel functions and bifurcating subcritically from $u = 0$ at $r = 0$; (*b*) a pair of target patterns, with maximum amplitude $\mathcal{O}(|r|^{1/2})$ away from the center, bifurcates subcritically from $u = 0$ at $r = 0$ for each $b_2 > b_2^* \equiv \sqrt{27/38}q_c^2$ (i.e., $a < 0$). Both spot A and the two target states snake when $b_2 > b_2^*$, at least initially; (*c*) there is a second family of spots (spot B) with negative $\mathcal{O}(|r|^{3/8})$ amplitude in the center
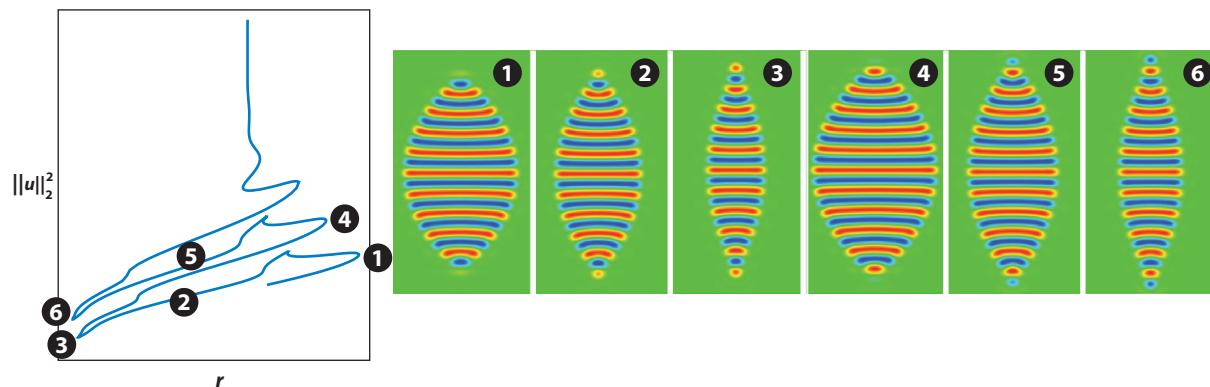

Figure 18

Planar leaf-like solutions of SH35 at the points labeled 1–6 in the left panel. Parameters: $b_3 = 2$, $q_c = 1$. Adapted from Reference 85. ©2010 Society for Industrial and Applied Mathematics. Adapted with permission. All rights reserved.
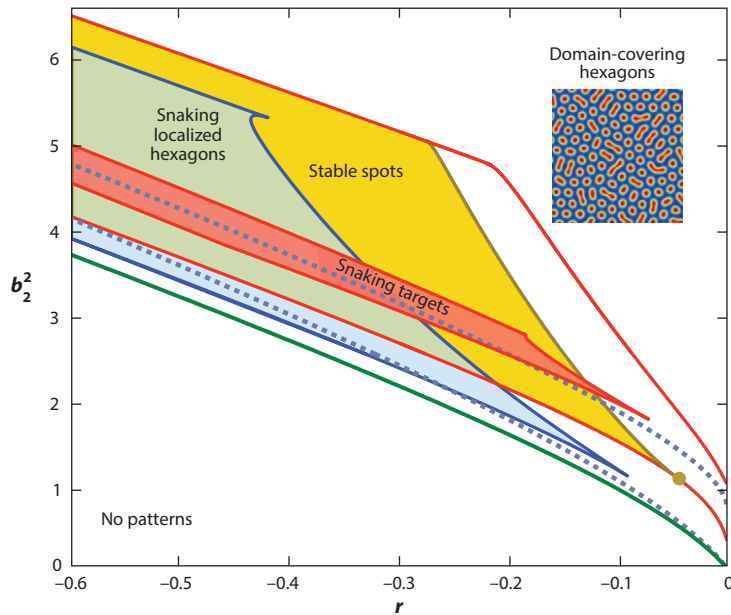
Figure 19

Location in the parameter plane of localized hexagons, targets, and spots in SH23 with $q_c = 1$. Adapted from Reference 86. ©2008 Society for Industrial and Applied Mathematics. Reprinted with permission. All rights reserved.

that bifurcates subcritically from $u = 0$ at $r = 0$ for each $b_2 > b_2^*$. However, snaking does not continue indefinitely—at large enough amplitude the structure breaks up into isolas as spot A reconnects with target A and spot B reconnects with target B. At yet larger amplitude the structures are so extended that the curvature effects near the outer front are reduced and snaking resumes. In contrast, spots consisting of one homogeneous state embedded within another do not snake.

The fact that spots A are present for $0 < b_2 < b_2^*$, i.e., in the absence of hysteresis between the homogeneous state and the 1D periodic state, could explain the prevalence of spots in experiments in which 1D bistability does not occur.

3.4. Secondary Snaking

Secondary snaking has been observed in several systems. In the 2D SH23, stripes of hexagons undergo primary snaking corresponding to the addition of complete rows of cells on either side of the stripe, but each row itself grows on an inhomogeneous interface, leading to secondary snaking associated with the nucleation of individual cells (86) (**Figure 20**). Other examples of similar behavior have been found in a reaction-diffusion model (89) and in 3D convection in a vertical slot (90). This type of behavior arises whenever growth processes in two distinct directions compete, e.g., x versus y growth, as in **Figure 20**, and radial versus azimuthal growth, as in Reference 89.

4. FLUID DYNAMICS

In fluid dynamics, multiple localized states were first identified in a vertical liquid-filled cavity driven by lateral gradients in temperature and concentration (13). Insights
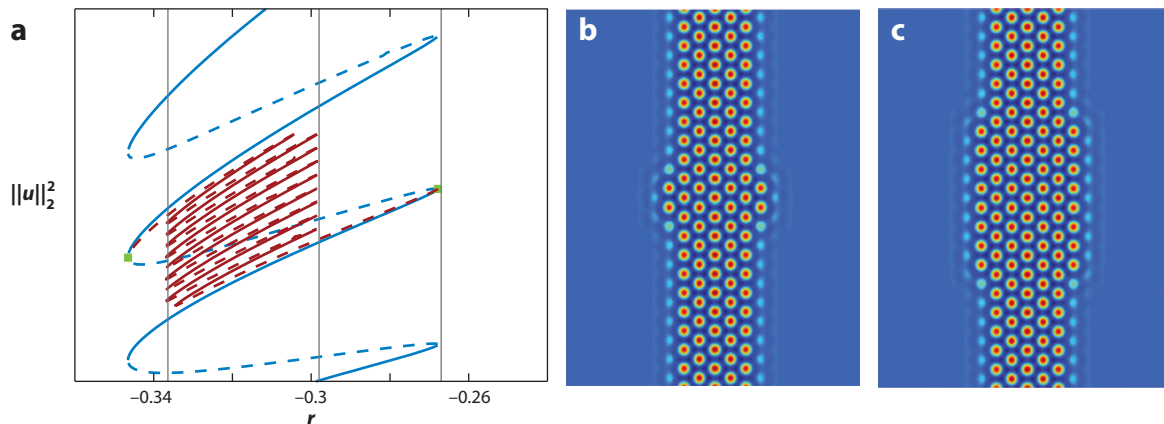
Figure 20

(*a*) Secondary snaking in SH23 associated with the growth of a new row of cells. (*b*,*c*) Sample solutions at $r = -0.3$ along the secondary snaking branch. Parameters: $b_2 = 1.6$, $q_c = 1$. Adapted from Reference 86. ©2008 Society for Industrial and Applied Mathematics. Reprinted with permission. All rights reserved.

based on the Swift-Hohenberg equation have led to a better understanding of this phenomenon.

For applications of these ideas to specific systems, one needs first to find a good approximation to the solution of the nonlinear problem to use as an initial guess for numerical continuation. This may be done in one of two ways: (*a*) solving the time-independent linear problem describing perturbations of a homogeneous state for the spatial eigenvalue λ and searching for purely imaginary eigenvalues of double multiplicity. In fluid mechanics, this typically requires the solution of a complex-valued boundary value problem. If such a parameter value is found and the corresponding periodic states bifurcate subcritically, the presence of localized states in the subcritical regime is guaranteed and the eigenfunctions in this regime provide a good approximation to these states that can be used to initialize numerical continuation (91). (*b*) In some problems, such as binary fluid convection and PCF, the periodic states come in from infinity, and in this case numerical integration in time is useful. This may identify a stable localized state that may then be followed using numerical continuation (2D binary fluid convection); alternatively, localized transients may be used to initialize numerical continuation (PCF). Numerical continuation of steady (or time-dependent) solutions is extremely useful since both stable and unstable states can be followed and the origin of stable states determined.

4.1. Binary Fluid Convection

The best-studied system from the above point of view is binary fluid convection with a negative separation ratio and identical boundary conditions at top and bottom. In this system, the heavier and lighter components of the mixture partially separate when the system is placed in an imposed temperature gradient. When the system is heated from below the heavier component migrates toward the hotter boundary at the bottom, and its effects on buoyancy then compete with the thermal effects, leading to an oscillatory doubly diffusive instability. This instability develops into traveling waves and in large domains generates a state known as dispersive chaos (92, 93). Simulations by Batiste et al. (14) have shown that as the Rayleigh number Ra increases, this

chaotic state itself undergoes a focusing instability that leads to the appearance of steady spatially localized convection, i.e., a convecton. This word, coined by A. Rucklidge, first appears in a paper by Blanchflower (94). The growth of the convecton suppresses motion in the rest of the domain, leading to numerically stable, localized convection embedded in a background conduction state. The stability of this state is a surprise because the background state is unstable to the oscillatory instability. Batiste et al. (14) suggest that this is a consequence of the interaction of the small amplitude traveling waves with the convectons. These absorb the waves for values of Ra for which a wavepacket propagates faster than it grows, i.e., for $Ra < Ra_a$, where Ra_a defines the threshold for absolute instability (95). The background therefore fills with waves only for $Ra > Ra_a$ (see 96).

The convectons found by Batiste et al. (14) are of odd and even parity and fall on intertwined branches, much as in SH35. This is a consequence of the symmetry of the binary fluid equations with respect to the layer midplane, and hence a consequence of the use of the Boussinesq approximation together with identical boundary conditions at the top and bottom boundaries. As a result new rolls are nucleated near the left edge of the snaking region and mature by the time Ra reaches the right edge. With each complete oscillation of the branch, the structure adds a pair of rolls, one roll on either side, just as in SH35. The rung states are also present (67) but correspond to asymmetric convectons that drift, a consequence of the nongradient structure of the fluid equations. Like the rung states in SH35, these are unstable. Since the rolls at either end of an odd parity state rotate in the same sense, the odd parity states entrain concentration-rich or concentration-poor fluid from one side of the structure and reject it at the other end: Odd parity convectons therefore act as a pump that transfers concentration from one side of the structure to the other. Since the direction of the end rolls reverses with each oscillation of the branch, the pumping direction also reverses. In contrast, the even structures entrain concentration-rich/concentration-poor fluid from both sides simultaneously and so are associated with enhanced/suppressed concentration relative to the mean. As one proceeds up the even convecton branch and the convectons add new rolls on either side, these processes alternate. Multipulse states have also been computed, and these behave as in SH35 (97).

In addition to calculations with periodic boundary conditions, calculations have also been done with Neumann boundary conditions (NBCs) at the sides and with no-slip, no-flux boundary conditions [insulating closed container boundary conditions (ICCBCs)]. The use of NBCs breaks translation invariance, and this results in the termination of the snaking branches on different branches. Since Eckhaus points remain multiple bifurcation points, the termination of a single branch of localized states is accompanied by the appearance of a non-snaking branch of defect-like states called mixed modes. Farther from the Eckhaus point, these states also resemble localized structures, leading to scenarios in which not all localized structures snake. Since NBCs allow discrete translations, it is possible to use these to construct localized solutions confined to the boundary and then use these to find similar solutions attached to walls in the case of ICCBCs (97). These wall-attached states also snake but because they are in effect localized states on a domain of double size, they snake with twice the frequency, as each oscillation is responsible for the addition of only one roll. These results provide a likely explanation for the states first identified by Ghorayeb & Mojtabi (13) in doubly diffusive convection in a vertical slot. No time-independent localized states have been found in binary convection in cylindrical domains despite the presence of a focusing instability analogous to that in two dimensions (98).

Similar single-pulse and multipulse snaking behavior has been found in 2D doubly diffusive convection in a horizontal layer (99) and in 2D binary convection in a porous medium (100). Recent extension of the latter study to 3D has revealed remarkable localized structures resembling

snowflakes in which the stationary structure sends out long arms, as one follows the solution branch, consisting of transverse rolls that appear to be confined laterally by the expulsion of concentration gradients from within the arms (101), in a manner reminiscent of the 1D process first described by Riecke (102).

4.1.1. Collisions. When the midplane symmetry R_2 of the system is broken, for example by allowing heat to leak out from the upper boundary, the odd parity convectons necessarily start to drift while R_1 symmetric states remain stationary. Given the large number of coexisting states of this type within the pinning region, different types of collisions are possible, but all turn out to be inelastic (67), as predicted by the corresponding problem using SH35 (66). Nishiura et al. (103, 104) have studied similar processes in reaction-diffusion equations in 1D and 2D. In these systems, localized spots exist as stable solutions, but these can undergo a parity-breaking bifurcation resulting in drift and hence collisions. Owing to the absence of snaking, all spots at a fixed parameter value are identical, but their interaction can lead to annihilation, repulsion, or coalescence into a single drifting pulse, depending on the parameters. Ward and colleagues (105, 106) have studied instabilities leading to spot fission and hence to spot proliferation, employing asymptotic techniques based on the assumed disparity in the diffusion coefficients of the activator and inhibitor to study the organization of the resulting spots in 2D. Studies of this type are motivated by experiments (107, 108), and in this case these were in turn motivated by simulations of model reaction-diffusion systems, such as the Gray-Scott model (109).

4.1.2. Localized traveling waves. It is important to distinguish spatially localized steady states that drift, such as that shown in **Figure 12c**, created by changing the temperature boundary condition at the top to allow heat loss (67) from superficially similar states created through a modulational instability of traveling wave convection. This type of time-dependent convection is characteristic of doubly diffusive systems, including binary fluid convection. The waves are created through a primary Hopf bifurcation and lead to wavepackets that drift with the group speed of the waves, a speed that differs in general from the phase speed of the waves within the wavepacket. Such states are therefore quasiperiodic, and the motion is driven by phase lag between the thermal and concentration fields (110). In experiments (111, 112) and simulations (110), waves of this type are found in the subcritical regime, i.e., below the primary Hopf bifurcation. In contrast, the drifting steady states are stationary in a comoving frame, and phase lags between the thermal and concentration fields are absent. At a fundamental level the mathematics behind the formation and evolution of localized traveling waves is not fully understood, although it is clearly related to a focusing instability and amplitude saturation via wavenumber growth (113). Heroic simulations of such waves have recently been carried out by Watanabe et al. (114; see also, 115).

4.2. Shear flows

Localized structures have been observed in experiments on the transition to turbulence for many years. In pipe flow, these take the form of spontaneously generated turbulent puffs that either decay as they propagate downstream or trigger a transition to turbulence (116). PCF, in which a shear flow is driven by horizontal plates moving with speed U in opposite directions, is better suited for studies of localization since the symmetry $R_1 \times R_2$ of this system forces structures with $R_1 \circ R_2$ symmetry to be stationary. PCF is known to be linearly stable for all Reynolds numbers $Re \equiv UL/\nu$, where $2L$ is the separation between the planes and ν is the kinematic viscosity (117).

However, like pipe flow, the flow is susceptible to finite amplitude perturbations that trigger the appearance of turbulence at values of Re as low as $Re \approx 325$ (80, 118, 119). For pipe flow, the corresponding value is $Re \approx 2,040$ (81). Numerical computations have revealed the presence of localized edge states, states lying on the boundary between laminar and turbulent PCF (16, 17). These states are localized in the spanwise (cross-stream) direction and are typically once unstable. When used to initialize numerical continuation, these states have been found to exhibit the type of snaking expected of systems with the symmetry of SH35. Odd states that are in as much contact with the upper and lower plates are stationary (EQ), but even states that have greater contact with either the upper or lower plate have a nonzero streamwise velocity (TW; **Figure 21**). The asymmetric rung states are also present (120). It is remarkable that after more than a century of study, ideas based on the Swift-Hohenberg equation have led to the discovery of a completely new class of solutions of this classic problem. In fact, localization in the spanwise direction is not surprising—it is a consequence of the pinning of the fronts bounding the structure to the streamwise-aligned vortices generated by finite amplitude perturbations. The streamwise localization of these structures, if any, is more problematic since it may have to rely on weak departures from two-dimensionality; strictly 2D structures are known to decay because of the absence of the self-sustaining mechanism identified by Waleffe (121). In such states, streamwise pinning would be absent in any case.

Although these states are unstable, experiments (80, 119) and simulations (122, 123) of PCF reveal a second type of localized state: localized stripes of turbulence at an oblique angle to the streamwise direction with nonturbulent shear flow in between. Despite our ability to simulate this remarkable state, its origin remains unclear. Models based on ideas from the theory of excitable systems have proved illuminating (124), but it may be that one should view the system as a bistable system with a stable homogeneous shear flow and a coexisting turbulent state, with the latter state undergoing a saddle-node bifurcation at $Re < 325$. Bifurcation to a state of spatially modulated turbulence from the saddle-node could lead to a turbulent state with nonturbulent "holes" that acquires stability as Re increases, much as occurs in similar situations arising in oscillon models (69).
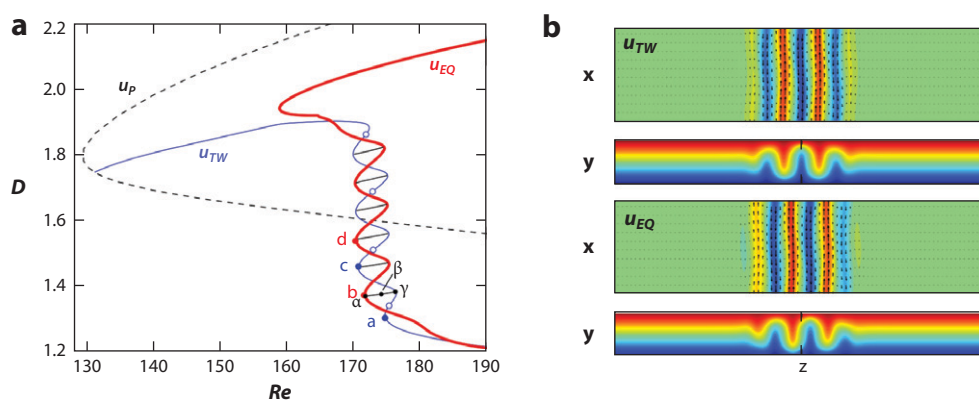

Figure 21

(*a*) Bifurcation diagram showing the snakes-and-ladders structure of localized states in plane Couette flow showing the dissipation D as a function of the Reynolds number Re. (*b*) Sample solutions u_{TW} (*top panels*) and u_{EQ} (*bottom panels*) showing the streamwise velocity in the midplane (*upper*) and the spanwise cross-section (*lower*). Adapted from Reference 120.

5. CONSERVED SYSTEMS

The above behavior is typical of nonconserved order parameter fields. However, an important subclass of gradient systems possesses a conserved quantity, and in such systems the order parameter field has a fixed mean value. Systems of this type arise frequently in fluid convection and other applications (125–127) and are distinguished from the standard scenario summarized above by the following properties (128, 129): (*a*) The snaking becomes slanted (sometimes referred to as sidewinding); (*b*) localized states may be present outside of the region of coexistence of the homogeneous and periodic states; and (*c*) localized states are present even when the periodic states bifurcate supercritically, i.e., when the coexistence region is absent entirely. The slanting of the snakes-and-ladders structure is a finite size effect: In a finite domain, expulsion of the conserved quantity from the localized states implies its excess outside, a fact that progressively delays (to stronger forcing) the nucleation events whereby the localized states grow in length. The net effect is that localized states are found in a much broader region of parameter space than in nonconserved systems.

5.1. Fluid Systems with a Conserved Quantity

Convection in an imposed magnetic field (130) provides a classic example of a system with a conserved quantity, the magnetic flux imposed across the layer. The conservation of flux is a consequence of the boundary conditions typically adopted for this type of problem and implies that the flow within the layer can at most redistribute the flux. The resulting conserved quantity exerts considerable influence on the behavior of the system, provided the system is of finite lateral extent. The presence of the conserved quantity implies that long wavelength perturbations of the conduction state are only weakly damped. This slow mode must therefore be included in the derivation of amplitude equations valid near the onset of the convective instability that sets in as Ra increases. This is also the case for 2D convection in a horizontal layer with stress-free boundaries at top and bottom that is rotating uniformly about the vertical $\hat{\mathbf{z}}$, where the conserved quantity is the zonal momentum $\int v(x,z)\mathrm{d}x\mathrm{d}z$ that may be set equal to zero (125). Here, v represents the y component of the velocity. The equations analogous to Equation 10 take the form

$$A_T = rA + A_{XX} - \frac{1}{2}\left(1 - \xi^2\right)|A|^2 A - \xi A V_X \qquad\qquad 16.$$

$$V_T = V_{XX} + \xi\left(|A|^2\right)_X \qquad\qquad 17.$$

(125, 131, 132), where ξ is a parameter measuring the strength of the magnetic field or rotation, and $X \equiv \epsilon x$, $T \equiv \epsilon^2 t$ are slow spatial and temporal variables. Here, the complex amplitude A represents the strength of the convective flow in the (x, z) plane, and V denotes the large-scale mode. It was realized by Cox & Matthews (125, 131) that the coupling to the large-scale mode destabilizes supercritical convection close to onset, resulting in the presence of spatially modulated states close to onset even in situations in which a hysteresis loop is absent. Despite earlier attempts (125, 133), the fully nonlinear states resulting from this instability have only been computed recently (126, 127). The calculations confirm that all three departures (*a–c*) from standard behavior mentioned above take place in these systems (**Figure 22**) and confirm that these are a consequence of the coupling to a large-scale mode. The magnetic convectons expel magnetic flux to the outside, while in the rotating layer the convectons expel gradients in the zonal velocity,

resulting in slower rotation within the localized structure and faster rotation outside. Thus, convectons are embedded in a shear layer they themselves create. These results are consistent with the weakly nonlinear theory summarized above. In the stationary case with periodic boundary conditions on the large scale X, Equation 17 implies that

$$V_X = \xi\left(\langle|A|^2\rangle - |A|^2\right),$$

18.

where $\langle\cdot\rangle$ represents a spatial average over the domain. Thus, $V_X > 0$ if $|A|^2 < \langle|A|^2\rangle$, i.e., outside the convecton, whereas $V_X < 0$ if $|A|^2 > \langle|A|^2\rangle$, i.e., inside the convecton, exactly as found in fully nonlinear computations (126, 127). Note that the resulting equation for A is nonlocal, with the effective Raleigh number $r_{eff} \equiv r - \xi^2\langle|A|^2\rangle$ responsible for the presence of a slant in the bifurcation diagram and any associated snaking. Nonlocal evolution equations of this type have been studied by a number of authors (134–136).

If the boundary conditions are perturbed in such a way as to destroy the conservation of the conserved quantity, the large-scale mode becomes damped and its characteristic scale becomes the convection length scale. Localized states remain, albeit at different values of the parameter, but snaking returns to its standard, nonslanted form (137). Related issues arise in studies of oscillons in granular media (or liquids), where the conservation of mass (or volume) also exerts a significant influence (138–141).
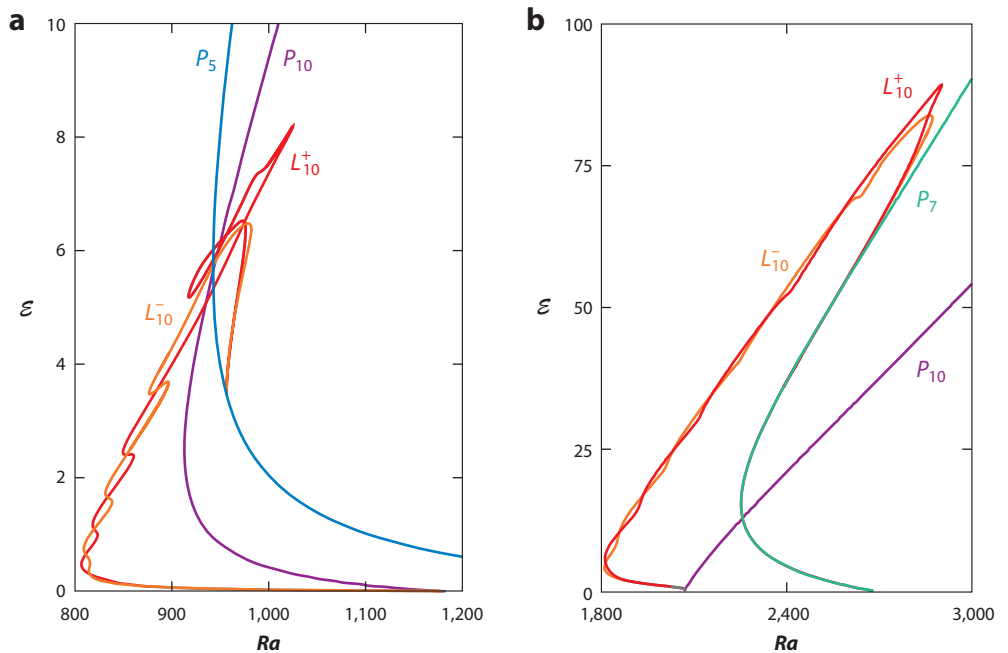

Figure 22

Poloidal kinetic energy $\mathcal{E}$ per unit area as a function of the Rayleigh number Ra showing slanted snaking in rotating convection. Bifurcation to subcritical localized states from (*a*) a subcritical branch P_{10} of periodic states with 10 wavelengths in the domain and (*b*) a supercritical P_{10} branch. Adapted from Reference 127.

5.2. The Conserved Swift-Hohenberg Equation and Phase-Field Crystals

The conserved Swift-Hohenberg (cSH) equation arguably provides the simplest illustration of the above results. Although this equation appears in earlier work in different fields (131, 142), it arises naturally in the phase-field crystal (PFC) model of soft matter (143). This model is in turn derived from the dynamical density functional theory (DDFT) of solids (143–145) and may be viewed as probably the simplest microscopic model for the freezing transition that can be constructed. In this model, the transition from a homogeneous state to a periodic state corresponds to the transition from a uniform density liquid to a periodic crystalline solid. The localized structures of interest in this model then correspond to states in which a finite size portion of the periodic crystalline phase coexists with the uniform density liquid phase, and these are expected to be present in the coexistence region between the two phases. In fact, it turns out that localized structures are also present at state points outside of the coexistence region (146). Some rather striking examples of localized structures in large 2D systems with conserved mass include snow-flake-like and dendritic structures (143, 147–149).

PFC: phase-field crystal

We write the cSH (or PFC) equation in the form

$$\partial_t \phi(\mathbf{x}, t) = \alpha \nabla^2 \frac{\delta F[\phi]}{\delta \phi(\mathbf{x}, t)}, \qquad F[\phi] \equiv \int d\mathbf{x} \left[\frac{\phi}{2} \left[r + \left(q_c^2 + \nabla^2 \right)^2 \right] \phi + \frac{\phi^4}{4} \right], \qquad 19.$$

where $\phi(\mathbf{x}, t)$ is an order parameter field that corresponds in the PFC context to a scaled density profile, r plays the role of temperature, and α is a (constant) mobility coefficient. It follows that the system evolves according to the cSH equation

$$\partial_t \phi = \alpha \nabla^2 \left[r\phi + \left(q_c^2 + \nabla^2 \right)^2 \phi + \phi^3 \right]. \qquad 20.$$

A cubic contribution can be added to F without substantial change in behavior. This is because the role of the coefficient b_2 is now played by ϕ_0, the conserved average value of the order parameter $\phi(\mathbf{x})$. Stationary states thus obey the equation

$$r\phi + \left(q_c^2 + \nabla^2 \right)^2 \phi + \phi^3 = \mu, \qquad 21.$$

where μ is the chemical potential for a supercooled liquid. The quantity ϕ_0 controls the fraction of the mass that is in the liquid and solid phases, and this fraction depends on the temperature $r < 0$. The bifurcation diagrams showing $\|\phi - \phi_0\|$ as a function of ϕ_0 take the form of slanted snaking (cf. **Figure 22**), complete with rung states representing asymmetric states, provided r is sufficiently below the thermodynamic tricritical point (146). It is significant that the localized states described by these diagrams tend to have lower energy than the periodic crystal and that standard snaking is recovered if the results are replotted as a function of μ (146). Thus, μ is the proper thermodynamic variable for systems of this type, and it would be of interest to identify a quantity that plays the role of the chemical potential in the fluid systems with conserved dynamics described above.

Direct numerical simulation of the cSH equation in 2D and 3D (146) reveals a similar thermodynamic preference for localized structures in particular intervals of ϕ_0. However, the significance of these states for the liquid-solid transition in soft matter systems remains to be worked out, as does the persistence of these structures in more realistic models of the particle-particle interaction, e.g., within a nonlocal description like DDFT.

DISCLOSURE STATEMENT

ACKNOWLEDGMENT

LITERATURE CITED

1. Korteweg DJ, de Vries G. 1895. *Philos. Mag.* 39:422–43
2. Zabusky NJ, Kruskal MD. 1965. *Phys. Rev. Lett.* 15:240–43
3. Ackemann T, Firth WJ, Oppo G-L. 2009. *Adv. At. Mol. Opt. Phys.* 57:323–421
4. Purwins H-G, Bödeker HU, Amiranashvili S. 2010. *Adv. Phys.* 59:485–701
5. Dawes JHP. 2010. *Philos. Trans. R. Soc. A* 368:3519–34
6. Knobloch E. 2008. *Nonlinearity* 21:T45–60
7. Cowley MD, Rosensweig RE. 1967. *J. Fluid Mech.* 30:671–88
8. Richter R, Barashenkov IV. 2005. *Phys. Rev. Lett.* 94:184503
9. Hunt GW, Peletier MA, Champneys AR, Woods PD, Ahmer Wadee M, et al. 2000. *Nonlinear Dyn.* 21:3–29
10. Vladimirov AG, McSloy JM, Skryabin DV, Firth WJ. 2002. *Phys. Rev. E* 65:046606
11. Strumpel C, Astrov YA, Purwins H-G. 2000. *Phys. Rev. E* 64:4889–97
12. Bortolozzo U, Clerc MG, Residori S. 2009. *New J. Phys.* 11:093037
13. Ghorayeb K, Mojtabi A. 1997. *Phys. Fluids* 9:2339–48
14. **Batiste O, Knobloch E, Alonso A, Mercader I. 2006. *J. Fluid Mech.* 560:149–58**
15. Gad-El-Hak M, Blackwelderf RF, Riley JJ. 1981. *J. Fluid Mech.* 110:73–95
16. Duguet Y, Schlatter P, Henningson DS. 2009. *Phys. Fluids* 21:111701
17. Schneider TM, Marinc D, Eckhardt B. 2010. *J. Fluid Mech.* 646:441–51
18. Laing C, Troy WC, Gutkin B, Ermentrout GB. 2002. *SIAM J. Appl. Math.* 63:62–97
19. Coullet P, Riera C, Tresser C. 2000. *Phys. Rev. Lett.* 84:3069–72
20. Yochelis A, Tintut Y, Demer LL, Garfinkel A. 2008. *New J. Phys.* 10:055002
21. Tlidi M, Lefever R, Vladimirov A. 2008. In *Lecture Notes in Physics*, Vol. 751, ed. B-G Englert, P Hänggi, W Hillebrandt, RAL Jones, H von Löhneysen, et al., pp. 1–22. New York: Springer
22. Meron E. 2012. *Ecol. Model.* 234:70–82
23. Lloyd DJB, O'Farrell H. 2013. *Phys. D* 253:23–39
24. Petrov V, Ouyang Q, Swinney HL. 1997. *Nature* 388:655–57
25. Umbanhowar PB, Melo F, Swinney HL. 1996. *Nature* 382:793–96
26. Lioubashevski O, Hamiel Y, Agnon A, Reches Z, Fineberg J. 1999. *Phys. Rev. Lett.* 83:3190–93
27. **Champneys AR. 1998. *Phys. D* 112:158–86**
28. Swift J, Hohenberg PC. 1977. *Phys. Rev. A* 15:319–28
29. Ma Y-P, Spiegel EA. 2011. *Phys. D* 240:150–65

14. First observation of homoclinic snaking in a fluid system

27. Key insight into the role of spatial reversibility and the presence of dissipative solitons in physics

30. Iooss G, Pérouème MC. 1993. *J. Differ. Equ.* 102:62–88
31. Burke J, Knobloch E. 2006. *Phys. Rev. E* 73:056211
32. Burke J, Knobloch E. 2007. *Chaos* 17:037102
33. Glebsky LY, Lerman LM. 1995. *Chaos* 5:424–31
34. Gaivão JP, Gelfreich V. 2011. *Nonlinearity* 24:677–98
35. Kozyreff G, Chapman SJ. 2006. *Phys. Rev. Lett.* 97:044502
36. Chapman SJ, Kozyreff G. 2009. *Phys. D* 238:319–54
37. Bensimon D, Shraiman BI, Croquette V. 1988. *Phys. Rev. A* 38:5461–64
38. Pomeau Y. 1986. *Phys. D* 23:3–11
39. Woods PD, Champneys AR. 1999. *Phys. D* 129:147–70
40. Burke J, Knobloch E. 2009. *Discret. Contin. Dyn. Syst.* 25(Suppl.):109–17
41. Beck M, Knobloch J, Lloyd DJB, Sandstede B, Wagenknecht T. 2009. *SIAM J. Math. Anal.* 41:936–72
42. Makrides E, Sandstede B. 2014. *Phys. D* 268:59–78
43. Knobloch J, Lloyd DJB, Sandstede B, Wagenknecht T. 2011. *J. Dyn. Differ. Equ.* 23:93–114
44. Burke JR. 2008. *Localized States in Driven Dissipative Systems*. PhD Thesis, Univ. Calif., Berkeley
45. Cross MC, Hohenberg PC. 1993. *Rev. Mod. Phys.* 65:851–1112
46. Hoyle RB. 2006. *Pattern Formation: An Introduction to Methods*. Cambridge, UK: Cambridge Univ. Press
47. van Saarloos W. 2003. *Phys. Rep.* 386:29–222
48. Aranson IS, Malomed BA, Pismen LM, Tsimring LS. 2000. *Phys. Rev. E* 62:R5–8
49. Bergeon A, Burke J, Knobloch E, Mercader I. 2008. *Phys. Rev. E* 78:046201
50. Dawes JHP. 2009. *SIAM J. Appl. Dyn. Syst.* 8:909–30
51. Houghton SM, Knobloch E. 2009. *Phys. Rev. E* 80:026210
52. Mercader I, Batiste O, Alonso A, Knobloch E. 2009. *Phys. Rev. E* 80:025201
53. Burke J, Houghton SM, Knobloch E. 2009. *Phys. Rev. E* 80:036202
54. Uecker H. 2001. *J. Nonlinear Sci.* 11:89–121
55. Kao H-C, Beaume C, Knobloch E. 2014. *Phys. Rev. E* 89:012903
56. Kozyreff G, Assemat P, Chapman SJ. 2009. *Phys. Rev. Lett.* 103:164501
57. Schmidt H, Hutt A, Schimansky-Geier L. 2009. *Phys. D* 238:1101–12
58. Clerc M, Falcon C. 2005. *Phys. A* 356:48–53
59. Yang J, Musslimani Z. 2003. *Opt. Lett.* 28:2094–96
60. Yulin AV, Champneys AR. 2010. *SIAM J. Appl. Dyn. Syst.* 9:391–431
61. Crawford JD, Knobloch E. 1991. *Annu. Rev. Fluid Mech*. 23:341–87
62. Burke J, Knobloch E. 2007. *Phys. Lett. A* 360:681–88
63. Dean AD, Matthews PC, Cox SM, King JR. 2011. *Nonlinearity* 24:3323–52
64. Burke J, Dawes JHP. 2012. *SIAM J. Appl. Dyn. Syst.* 11:261–84
65. Kozyreff G, Tlidi M. 2007. *Chaos* 17:037103
66. Houghton SM, Knobloch E. 2011. *Phys. Rev. E* 84:016204
67. Mercader I, Batiste O, Alonso A, Knobloch E. 2013. *J. Fluid Mech*. 722:240–66
68. Ma Y-P. 2011. *Localized Structures in Forced Oscillatory Systems*. PhD Thesis, Univ. Calif., Berkeley
69. Burke J, Yochelis A, Knobloch E. 2008. *SIAM J. Appl. Dyn. Syst.* 7:651–711
70. Ma Y-P, Burke J, Knobloch E. 2010. *Phys. D* 239:1867–83
71. Champneys AR, Knobloch E, Ma Y-P, Wagenknecht T. 2012. *SIAM J. Appl. Dyn. Syst.* 11:1583–613
72. Ma Y-P, Knobloch E. 2012. *Chaos* 22:033101
73. Lugiato LA, Lefever R. 1987. *Phys. Rev. Lett.* 58:2209–11
74. Mandel P, Georgiou M, Erneux T. 1993. *Phys. Rev. A* 47:4277–86
75. Alnahdi AS, Niesen J, Rucklidge AM, Wagenknecht T. 2014. *SIAM J. Appl. Dyn. Syst.* 13:1328–51
76. Verschueren N, Bortolozzo U, Clerc MG, Residori S. 2013. *Phys. Rev. Lett.* 110:104101
77. Kuramoto Y, Battogtokh D. 2002. *Nonlinear Phenom. Complex Syst.* 5:380–85
78. Abrams DM, Strogatz SH. 2004. *Phys. Rev. Lett.* 93:174102
79. Xie J, Knobloch E, Kao H-C. 2014. *Phys. Rev. E* 90:022919
80. Prigent A, Grégoire G, Chaté H, Dauchot O, van Saarloos W. 2002. *Phys. Rev. Lett.* 89:014501

30. Analysis of the normal form for the reversible Hopf bifurcation with 1:1 resonance

31. Elucidation of the snakes-and-ladders structure of the pinning region

36. Detailed beyond-all-orders asymptotics for SH23

38. First qualitative argument for the presence of the pinning region

41. A mathematical explanation of the snakes-and-ladders structure of the pinning region

81. Avila K, Moxey D, de Lozar A, Avila M, Barkley D, Hof B. 2011. *Science* 333:192–96
82. Duguet Y, Schlatter P, Henningson DS, Eckhardt B. 2012. *Phys. Rev. Lett.* 108:044501
83. Sakaguchi H, Brand HR. 1996. *Phys. D* 97:274–85
84. Clerc MG, Falcon C, Tirapegui E. 2005. *Phys. Rev. Lett.* 94:148302
85. Avitabile D, Lloyd DJB, Burke J, Knobloch E, Sandstede B. 2010. *SIAM J. Appl. Dyn. Syst.* 9:704–33

86. Detailed study of the growth of localized structures with hexagonal coordination

86. Lloyd DJB, Sandstede B, Avitabile D, Champneys AR. 2008. *SIAM J. Appl. Dyn. Syst.* 7:1049–100
87. Lloyd DJB, Sandstede B. 2009. *Nonlinearity* 22:485–524
88. McCalla S, Sandstede B. 2010. *Phys. D* 239:1581–92
89. Uecker H, Wetzel D. 2014. *SIAM J. Appl. Dyn. Syst.* 13:94–128
90. Beaume C, Bergeon A, Knobloch E. 2013. *Phys. Fluids* 25:024105
91. Bergeon A, Knobloch E. 2008. *Phys. D* 237:1139–50
92. Bretherton CS, Spiegel EA. 1983. *Phys. Lett. A* 96:152–56
93. Kolodner P, Glazier JA, Williams H. 1990. *Phys. Rev. Lett.* 65:1579–82
94. Blanchflower S. 1999. *Phys. Lett. A* 261:74–81
95. Tobias S, Proctor MRE, Knobloch E. 1998. *Phys. D* 113:43–72
96. Kolodner P. 1993. *Phys. Rev. E* 48:R665–68
97. Mercader I, Batiste O, Alonso A, Knobloch E. 2011. *J. Fluid Mech.* 667:586–606
98. Mercader I, Alonso A, Batiste O. 2008. *Phys. Rev. E* 77:036313
99. Beaume C, Bergeon A, Knobloch E. 2011. *Phys. Fluids* 23:094102
100. Lo Jacono D, Bergeon A, Knobloch E. 2010. *Phys. Fluids* 22:073601
101. Lo Jacono D, Bergeon A, Knobloch E. 2013. *J. Fluid Mech.* 730:R2
102. Riecke H. 1992. *Phys. Rev. Lett.* 68:301–4
103. Nishiura Y, Teramoto T, Ueda K-I. 2003. *Chaos* 13:962–72
104. Nishiura Y, Teramoto T, Ueda K-I. 2005. *Chaos* 15:047509
105. Chen W, Ward MJ. 2011. *SIAM J. Appl. Dyn. Syst.* 10:582–666
106. Iron D, Rumsey J, Ward MJ, Wei J. 2014. *J. Nonlinear Sci.* 24:857–912
107. Lee K, McCormick WD, Pearson JE, Swinney HL. 1994. *Nature* 369:215–18
108. Vanag VK, Epstein IR. 2007. *Chaos* 17:037110
109. Pearson JE. 1993. *Science* 216:189–92
110. Barten W, Lücke M, Kamps M, Schmitz R. 1995. *Phys. Rev. E* 51:5662–80
111. Kolodner P. 1991. *Phys. Rev. Lett.* 66:1165–68
112. Kolodner P. 1991. *Phys. Rev. A* 44:6466–79
113. Popp S, Stiller O, Kuznetsov E, Kramer L. 1998. *Phys. D* 114:81–107
114. Watanabe T, Iima M, Nishiura Y. 2012. *J. Fluid Mech.* 712:219–43
115. Taraut AV, Smorodin BL, Lücke M. 2012. *New J. Phys.* 14:093055
116. Willis AP, Kerswell RR. 2007. *Phys. Rev. Lett.* 98:014501
117. Romanov VA. 1973. *Funct. Anal. Appl.* 7:137–46
118. Manneville P. 2004. *Theor. Comput. Fluid Dyn.* 18:169–81
119. Prigent A, Dauchot O. 2005. In *IUTAM Symposium on Laminar-Turbulent Transition and Finite Amplitude Solutions*, ed. T Mullin, R Kerswell, pp. 193–217. Dordrecht, Neth.: Springer

120. Discovery of the snakes-and-ladders structure in plane Couette flow

120. Schneider TM, Gibson JF, Burke J. 2010. *Phys. Rev. Lett.* 104:104501
121. Waleffe F. 1997. *Phys. Fluids* 9:883–900
122. Barkley D, Tuckerman LS. 2005. *Phys. Rev. Lett.* 94:014502
123. Tuckerman LS, Barkley D. 2011. *Phys. Fluids* 23:041301
124. Barkley D. 2011. *Phys. Rev. E* 84:016309
125. Cox SM, Matthews PC. 2001. *Phys. D* 149:210–29
126. Lo Jacono D, Bergeon A, Knobloch E. 2011. *J. Fluid Mech.* 687:595–605
127. Beaume C, Bergeon A, Kao H-C, Knobloch E. 2013. *J. Fluid Mech.* 717:417–48
128. Firth WJ, Columbo L, Scroggie AJ. 2007. *Phys. Rev. Lett.* 99:104503
129. Dawes JHP. 2008. *SIAM J. Appl. Dyn. Syst.* 7:186–206
130. Weiss NO, Proctor MRE. 2014. *Magnetoconvection*. Cambridge, UK: Cambridge Univ. Press
131. Matthews PC, Cox SM. 2000. *Nonlinearity* 13:1293–320

132. Komarova NL, Newell AC. 2000. *J. Fluid Mech.* 415:285–321
133. Dawes JHP. 2007. *J. Fluid Mech.* 570:385–406
134. Hall P. 1984. *Phys. Rev. A* 29:2921–23
135. Elmer FJ. 1988. *Phys. D* 30:321–42
136. Vega JM. 2005. *Nonlinearity* 18:1425–41
137. Beaume C, Kao H-C, Knobloch E, Bergeon A. 2013. *Phys. Fluids* 25:124105
138. Tsimring LS, Aranson IS. 1997. *Phys. Rev. Lett.* 79:213–16
139. Eggers J, Riecke H. 1999. *Phys. Rev. E* 59:4476–83
140. Winterbottom DM, Cox SM, Matthews PC. 2008. *SIAM J. Appl. Dyn. Syst.* 7:63–78
141. Dawes JHP, Lilley S. 2010. *SIAM J. Appl. Dyn. Syst.* 9:238–60
142. Knobloch E. 1989. *Phys. Rev. A* 40:1549–59
143. Emmerich H, Löwen H, Wittkowski R, Gruhn T, Tóth G, et al. 2012. *Adv. Phys.* 61:665–743
144. van Teeffelen S, Backofen R, Voigt A, Löwen H. 2009. *Phys. Rev. E* 79:051404
145. Archer AJ, Robbins MJ, Thiele U, Knobloch E. 2012. *Phys. Rev. E* 86:031603
146. **Thiele U, Archer AJ, Robbins MJ, Gomez H, Knobloch E. 2013. *Phys. Rev. E* 87:042915**
147. Pusztai T, Tegze G, Tóth GI, Kornyei L, Bansel G, et al. 2008. *J. Phys. Condens. Matter* 20:404205
148. Tegze G, Gránásy L, Tóth GI, Podmaniczky F, Jaatinen A, et al. 2009. *Phys. Rev. Lett.* 103:035702
149. Tegze G, Gránásy L, Tóth GI, Douglas JF, Pusztai T. 2011. *Soft Matter* 7:1789–99

146. Detailed study of the conserved Swift-Hohenberg equation

Contents

Errata

An online log of corrections to *Annual Review of Condensed Matter Physics* articles may be found at http://www.annualreviews.org/errata/conmatphys